A Multi-algorithm Approach for Modeling Coastal Wetland Eco-geomorphology

Zeli Tan[1*], L. Ruby Leung[1], Chang Liao[1], Luca Carniello[2], José F. Rodríguez[3], Patricia M. Saco[3], Steven G. Sandi[4]

[1]Pacific Northwest National Laboratory, Richland, WA, USA

[2]Department of Civil, Environmental and Architectural Engineering, University of Padova, Padova, Italy

[3]School of Engineering, University of Newcastle, Callaghan, Australia

[4]School of Engineering, Deakin University, Geelong, Australia

*Correspondence to: Zeli Tan (zeli.tan@pnnl.gov)

Abstract: Coastal wetlands play an important role in the global water and biogeochemical cycles. Climate change is making them more difficult to adapt to the fluctuation of sea levels and other environment changes. Given the importance of eco-geomorphological processes for coastal wetland resilience, many eco-geomorphology models differing in complexity and numerical schemes have been developed in recent decades. But their divergent estimates on the response of coastal wetlands to climate change indicate that substantial structural uncertainties exist in these models. To investigate the structural uncertainty of coastal wetland eco-geomorphology models, we developed a multi-algorithm model framework of eco-geomorphological processes, such as mineral accretion and organic matter accretion, within a single hydrodynamics model. The framework is designed to explore possible ways to represent coastal wetland eco-geomorphology in Earth system models and reduce the related uncertainties in global applications. We tested this model framework at three representative coastal wetland sites: two saltmarsh wetland (Venice Lagoon and Plum Island Estuary) and a mangrove wetland (Hunter Estuary). Through the model-data comparison, we showed the importance to use a multi-algorithm ensemble approach for more robust predictions of the evolution of coastal wetlands. We also find that more observations of mineral and organic matter accretion at different elevations of coastal wetlands and evaluation of the coastal wetland models at different sites of diverse environments can help reduce the model uncertainty.

Plain Language Summary: Coastal wetlands are a critical component of the earth system, strongly influencing global water and biogeochemical cycles. Although numerical models of coastal wetlands differ substantially in complexity and numerical methods, few studies have investigated the structural uncertainties of these models in a state-of-the-art way. To bridge this gap, we developed a multi-algorithm model framework for the eco-geomorphological processes

of coastal wetlands within a single hydrodynamics model. Through model-data comparison at three representative saltmarsh and mangrove sites, we demonstrated the importance to use a multi-algorithm ensemble approach for more robust predictions of the evolution of coastal wetlands. We also show the importance to include more comprehensive eco-geomorphology observations (e.g., observations along an elevation gradient and at different sites of diverse environments) for reducing the model uncertainty.

1. Introduction

Coastal wetlands, such as tidal marshes and mangroves, are valued for providing many important ecosystem services, including coastline protection, storm surge attenuation, wildlife habitat, and water quality improvement. Particularly, they are observed to sequester atmospheric carbon dioxide at a rate much higher than other ecosystems, thus offering a potential nature-based solution for climate mitigation (Aburto-Oropeza et al., 2008; Macreadie et al., 2019; Temmerman et al., 2013; Teuchies et al., 2013). Despite the resilience of coastal wetlands to past fluctuations in sea level and climate over long periods of time (Cahoon et al., 2006; Saintilan et al., 2020; Törnqvist et al., 2020), recent observations of local wetland loss raise concerns over their acclimation to intensified natural and human-induced disturbances, such as sea level rise (SLR), storm surge, sediment supply reduction, eutrophication and drought (Blum & Roberts, 2009; Crosby et al., 2016; Deegan et al., 2012; Kirwan & Megonigal, 2013; Törnqvist et al., 2021).

Eco-geomorphological processes, such as mineral accretion, organic matter (OM) accretion, landward migration and wave-action erosion, play crucial roles in the acclimation of coastal wetlands to natural and human-induced disturbances (Craft et al., 2009; Howes et al.,

2010; Kirwan et al., 2016; Leonardi et al., 2016; Schuerch et al., 2018). Mineral accretion is a process of mineral sediment accumulation on the soil bed of coastal wetlands through either plant-mediated particle settling or direct capture of sediment by plant stems (Kirwan & Mudd, 2012) and can help coastal wetlands build the elevation against rising sea levels (Cahoon et al., 2021). With the accumulation of plant litter in the soil column, OM accretion can also help raise the bed elevation of coastal wetlands (Kirwan & Mudd, 2012). Wave-action erosion can accelerate the land loss at the shore which reduces the habitat area of coastal wetlands (Leonardi et al., 2016). In contrast, landward migration is a process by which coastal wetlands move to higher elevation and expand their habitat area (Schuerch et al., 2018). Due to the importance of these eco-geomorphologic processes, many eco-geomorphology models different in complexity and parameterization methods have been developed in recent decades (D'Alpaos et al., 2011; Fagherazzi et al., 2012; Kirwan et al., 2010; Marani et al., 2007; Mcleod et al., 2010; Rodríguez et al., 2017). The application of these models at the regional, continental, and global scales have greatly advanced our understanding in the evolution of coastal wetlands under intensified environmental changes and provided valuable insights on the management and conservation of this ecosystem (Kirwan & Mudd, 2012; Leonardi et al., 2016; Mariotti & Fagherazzi, 2010; Reyes et al., 2000).

However, substantial structural uncertainty exists in these eco-geomorphology models as indicated by their inconsistent predictions on the fate of coastal wetlands under accelerated SLR (Craft et al., 2009; Kirwan et al., 2010, 2016; Rodríguez et al., 2017; Schuerch et al., 2018). For example, based on the Sea Level Affecting Marshes Model (SLAMM) that simulates the dominant processes (e.g., inundation, wave-action erosion, and salinity intrusion) but ignores the adaptation of salt marshes to SLR with accelerating rates of elevation change, Craft et al. (2009)

estimated that salt marshes will decline in area by 45% by 2100 under the worst Intergovernmental Panel on Climate Change (IPCC) SLR scenario. But based on a salt marsh model that represents the dynamic, eco-geomorphic feedbacks between tidal inundation and increased vertical accretion of mineral and organic sediments, a more recent study demonstrated that marshes could survive under a wide range of future SLR scenarios by building elevation at rates similar to or exceeding historical SLR (Kirwan et al., 2016). The structural uncertainty of the eco-geomorphology models has two sources. First, different eco-geomorphology models usually implement different parameterization schemes for the same process. For instance, there are at least seven different mineral accretion schemes implemented in various eco-geomorphology models (D'Alpaos et al., 2007; Fagherazzi et al., 2007; French, 2006; Kirwan & Mudd, 2012; Morris et al., 2012; Temmerman et al., 2003b; van de Koppel et al., 2005). Second, very few eco-geomorphology models include all eco-geomorphologic processes critical to the dynamics of coastal wetlands. As stated above, the SLAMM model used by Craft et al. (2009) does not include the dynamic, eco-geomorphic feedbacks between tidal inundation and increased vertical accretion of mineral and organic sediments. Moreover, the landward migration of coastal wetlands and its limitation by human barriers have not been represented in eco-geomorphology models until very recently (Schuerch et al., 2018).

To date, our understanding of the structural uncertainty of eco-geomorphology models is still limited, despite the importance of eco-geomorphological processes to the Earth system (Ward et al., 2020). A few studies have strived to understand the uncertainty of coastal wetland eco-geomorphology models through model comparison (Kirwan et al., 2010) or model review (Fagherazzi et al., 2012; Mcleod et al., 2010). However, unlike the state-of-the-art methods used to compare some other Earth system processes (Guseva et al., 2020; Huntzinger et al., 2013; Jin

et al., 2016; Schellnhuber et al., 2014; Tan et al., 2018), model comparison and review can only provide an incomplete evaluation of model uncertainty (Fisher & Koven 2020). For model review, the related studies mostly focused on analyzing high-level features of eco-geomorphology models, such as capability and complexity, inputs requirements, spatial- and temporal-scale accountability, and practical applicability, but did not consider the real performance of the eco-geomorphology models in simulating coastal wetland dynamics under diverse environmental conditions (Fagherazzi et al., 2012; Mcleod et al., 2010). For model comparison, previous studies usually performed the comparison of eco-geomorphology models at the ecosystem level with a focus on the overall response of coastal wetlands to SLR and the participant models were commonly not configured under a consistent protocol. As a result, the model uncertainty associated with individual processes cannot be isolated and not all estimated model uncertainty can be attributed to eco-geomorphologic processes (Kirwan et al., 2010). In addition, these model comparison studies were only conducted at specific or very few sites (Kirwan et al., 2010). It is thus unclear how well the knowledge gained at a specific site can be transferred to other environmental conditions.

Algorithm-level model comparison approaches have shown promising skills for assessing the uncertainty of a particular process in large-scale models (Donatelli et al., 2014; Jin et al., 2016; Tan et al., 2018). Motivated by these studies, we developed an algorithm-level model comparison framework to investigate the structural uncertainty of coastal wetland eco-geomorphology models. The framework's efficacy is evaluated at the coastal wetland sites of distinct environmental conditions. Through this work, we aim to evaluate the algorithm-level uncertainties of coastal wetland eco-geomorphology modeling related to mineral and OM accretion and explore possible ways to reduce the related uncertainties in global applications.

2. Materials and methods

2.1. Model description

We developed a Multi-Algorithm Coastal wetland Eco-geomorphology Simulator (MACES) model framework to assess the structural uncertainty of eco-geomorphology models. The MACES framework consists of two components (Figure 1): a one-dimensional (1-D) transect-based hydrodynamic module (MACES-hydro) and an algorithm-level model comparison module that implements different eco-geomorphologic process algorithms (MACES-geomor). MACES-hydro simulates water level, tide velocity, significant wave height, bottom shear stress, suspended sediment and other hydrodynamic conditions along a 1-D coastal transect that varies from low-elevation open water at the ocean side to high-elevation upland at the land side (Figure 2). All eco-geomorphology algorithms in MACES-geomor (Table 1) use the same hydrodynamic conditions simulated by MACES-hydro to model eco-geomorphologic processes, such as mineral and OM accretion, at each grid cell of the coastal transect. At the end of each year, MACES updates the transect elevation profile and land cover. A design feature of MACES is that a new coastal wetland eco-geomorphology model can be easily created by configuring MACES-geomor with a different combination of eco-geomorphologic algorithms. Although we focus on mineral and OM accretion in this work, the developed framework can be extended to other eco-geomorphologic processes, such as landward migration and wave-action erosion. Landward migration and wave-action were not tested for this study due to data limitations.

The 1D transect-based coastal hydrodynamics model MACES-hydro was developed mainly based on the work of Tambroni & Seminara (2012) and Carniello et al. (2005) for cross-section averaged physical variables on the coastal landscape. It simulates tide and storm surge

propagation, wave generation and propagation, and particle transport. Tide and storm surge driven water flow is governed by the 1-D Saint Venant Equations (Tambroni & Seminara, 2012):

$$\frac{\partial h}{\partial t} + \frac{\partial (Uh)}{\partial x} = 0, \quad (1)$$

$$\frac{\partial U}{\partial t} + U\frac{\partial U}{\partial x} + g\frac{\partial H}{\partial x} + g\frac{U|U|}{C_z^2 h} = 0, \quad (2)$$

where h is water flow depth (m), U is water flow velocity (m s^{-1}), H is water surface elevation (m) relative to the Mean Sea Level (MSL), g is the acceleration due to gravity (m^2 s^{-1}), and C_z is the Chézy's friction coefficient ($m^{1/2}$ s^{-1}). The friction coefficient C_z is a function of bed roughness, vegetation stem size and vegetation density, described in detail in Section 1.1 of Text S1. Wave generation and propagation in shallow waters is described by the conservation of the wave action N, which is defined as the ratio of wave energy E (J m^{-2}) to the relative wave frequency σ. By using the linear wave theory, the wave action conservation equation can be simplified as (Carniello et al., 2005):

$$\frac{\partial N}{\partial t} + \frac{\partial (c_g N)}{\partial x} = \frac{S}{\sigma}. \quad (3)$$

The wave group celerity c_g is given as (Mariotti & Fagherazzi, 2010):

$$c_g = \frac{\sigma}{2k}\left(1 + \frac{2kh}{\sinh(2kh)}\right), \quad (4)$$

where k is the wave number ($k = 2\pi/\lambda$, where λ is wavelength). The wave energy source term S is determined by the wind wave generation S_{wg}, the wind wave dissipation through bottom friction S_{bf}, the white capping S_{wc}, and the depth induced breaking S_{brk}:

$$S = S_{wg} - S_{bf} - S_{wc} - S_{brk}. \quad (5)$$

The detailed definitions of the gain and loss terms of wave energy can be found in Section 1.2 of Text S1. Both tide and storm surge induced water flow and wind induced waves contribute to the production of bottom shear stress τ_b, which is important for the modeling of sediment deposition

and resuspension over the coastal landscape. Suggested by Soulsby (1997), the nonlinear interaction between these two forces can be evaluated using the below empirical formulation:

$$\tau_b = \tau_{wave} + \tau_{curr}\left[1 + 1.2\left(\frac{\tau_{wave}}{\tau_{curr}+\tau_{wave}}\right)^{3.2}\right], \quad (6)$$

where τ_{curr} is the bottom shear stress induced by water flow only and τ_{wave} is the bottom shear stress induced by wave only. As detailed in Section 1.3 of Text S1, the shear stress τ_{curr} is a function of water flow velocity U and water depth h and the shear stress τ_{wave} is a function of significant wave height H_w, water depth h and wave period T. The transport of suspended sediment in the water column is governed by the advection-dispersion continuity equation (Maan et al., 2015):

$$\frac{\partial c_{ss}h}{\partial t} + \frac{\partial (U c_{ss} h)}{\partial x} - \frac{\partial}{\partial x}\left(Kh\frac{\partial c_{ss}}{\partial x}\right) = -Q_m, \quad (7)$$

where c_{ss} is the depth-averaged suspended sediment concentration (SSC) (kg m^{-3}), K is the dispersion coefficient (m^2 s^{-1}), and Q_m is the net sediment deposition rate (kg m^{-2} s^{-1}). The net sediment deposition is defined as sediment deposition minus sediment resuspension and the long-term average of Q_m equals to mineral accretion. For salinity and nutrients, it is assumed that their concentrations do not change during transport over the coastal landscape and thus the dynamics are directly controlled by inundation.

As listed in Table 1, MACES-geomor implements seven widely used algorithms for mineral accretion (D'Alpaos et al., 2007; Fagherazzi et al., 2007; French, 2006; Kirwan & Mudd, 2012; Morris et al., 2012; Temmerman et al., 2003b; van de Koppel et al., 2005) and four algorithms for OM accretion (D'Alpaos et al., 2007; Kakeh et al., 2016; Kirwan & Mudd, 2012; Morris et al., 2012), respectively. Correspondingly, the change of transect elevation η (m) is calculated using the Exner equation:

$$(1-\lambda)\frac{d(\rho_s \eta)}{dt} = Q_m + Q_{om}, \quad (8)$$

where λ is the sediment porosity, ρ_s is the sediment wet bulk density (kg m^{-3}), and Q_{om} is the OM accretion rate (kg m^{-2} s^{-1}). The detailed descriptions of these eco-geomorphologic algorithms can be found in Sections 2 and 3 of Text S1. It should be noted that for OM accretion, we included one more algorithm corresponding to the null hypothesis that OM accretion is negligible for the transect elevation change. Here, the algorithms of mineral and OM accretion were selected based on three criteria through literature review. First, the selected algorithms must have been successfully applied in multiple studies (ideally for coastal wetlands in different environmental conditions). Second, the selected algorithms are substantially different between each other in mathematical formulations and conceptual understanding. Third, the selected algorithms can be implemented using 1-D hydrodynamics. Table 1 summarizes all the MACES-geomor algorithms and their characteristics. The free parameters of mineral and OM accretion algorithms are listed in Tables S1 and S2, respectively.

We chose the 1-D hydrodynamic model over more advanced two-dimensional (2-D) or three-dimensional (3-D) hydrodynamic models (e.g., Delft3D) that can resolve detailed coastal hydrodynamics for two reasons. First, the prominent features of coastal wetlands that 2-D and 3-D hydrodynamic models can represent, such as tidal channels and microtopography, are usually at spatial scales of meters, which are much finer than the spatial resolutions that current and even future Earth system models (ESMs) can afford (Feng et al., 2022; Ward et al., 2020). Second, detailed 2-D and 3-D hydrodynamic models usually require intense labor work of mesh delineation to ensure model stability. As a result, it is difficult to configure such advanced models at continental or global scales, particularly when coupling them with eco-geomorphology models which dynamically alter the mesh bottom elevation. Third, while it is possible to model

eco-geomorphology at continental or global scales using simplified 2-D hydrodynamics models which do not resolve water flow and wave dynamics and only use semi-analytical approaches for suspended sediment is possible (Langston et al., 2020), the adoption of such 2-D approximations would exclude many widely used eco-geomorphic algorithms for comparison as they need water flow and wave as inputs (Cao et al., 2021; D'Alpaos et al., 2007; Leonardi et al., 2016). It should be noted that testing the applicability of multiple eco-geomorphologic algorithms on the same hydrodynamics platform is not new. For example, Delft3D has already implemented different mineral accretion algorithms in its morphodynamic module D-Morphology (Deltares, 2022). But as discussed above, compared to these models, our work is more relevant to representing coastal wetland geomorphology in ESMs. Moreover, our multi-algorithm framework extends the comparison of eco-geomorphologic algorithms to biogeochemical and ecological processes, such as OM accretion, which are usually not included in 2-D and 3-D coastal models (Zhang et al., 2020). It should also be noted that, because 1-D hydrodynamics models do not represent channel processes, the 1-D discretization does not entirely preserve the site characteristics. As such, it is recognized that the MACES simulated hydrodynamics can provide less detail than 2-D and 3-D coastal models, however, as discussed above the results obtained in MACES are satisfactory for the purposes of Earth system modeling.

2.2. Numerical methods

We employed a 1-D Godunov-type central-upwind scheme (Kurganov & Levy, 2002) to discretize the spatial domain of the Saint Venant equations which include source terms due to bottom topography, the wave equation and the particle transport equation. This finite volume scheme introduces a linear piecewise approximation to each grid cell with the Superbee slope limiter (Roe, 1986) to achieve the solutions of both second-order accuracy in space and

diminishing total variation. Because this scheme is very effective in suppressing spurious oscillation of the simulated water level at the periodically flooded areas, it has been widely used as the numerical solver for coastal hydrodynamics (Liang & Marche, 2009). After spatial discretization, we employed a fourth-order adaptive Runge-Kutta-Fehlberg method to discretize the hydrodynamic equations in the time domain to achieve second-order accuracy in time (Burden et al., 1978). In addition, to avoid negative particle concentrations, we incorporated a scheme described by Tan et al. (2015) into the Runge-Kutta-Fehlberg method to recursively curtail the running time step when large negative concentrations occur, until the negative values are small enough to be assigned safely as zero.

One prominent feature of MACES is the use of a hybrid Fortran and Python programming approach to balance computational efficiency and software usability. The computational-intensive hydrodynamic module was written in Fortran and then converted to a Python package using f2py (Python Software Foundation, Fredericksburg, VA, USA). All the other modules, including eco-geomorphology, I/O and settings, were written in Python 3 directly. As such, new algorithms of eco-geomorphology can be easily integrated into MACES in the future. Model input and output files are written in the NetCDF and Excel format and model settings are written in the user-friendly XML (Extensible Markup Language) format.

2.3. Model calibration and evaluation

Model calibration of different MACES-geomor algorithms is conducted using the Python-version Parameter ESTimation tool (PyPEST). The PyPEST tool was developed by Liao et al. (2019) based on the model-independent parameter estimation code PEST (Doherty et al., 1994). PyPEST carries out the calibration process iteratively with six steps (parameter generation, model configuration, input data generation, model run in parallel, output extraction, and output

post-processing) until the user-defined cost function threshold criteria are met (Figure S1). Depending on data availability at different sites, different combinations of observed datasets are used to calibrate different geomorphology module algorithms with consideration of module dependency. For example, observed long-term mineral accretion rate and SSC are used to calibrate the mineral accretion algorithms. Observed long-term OM accretion rate and aboveground biomass are used to calibrate the OM accretion algorithms. When calibrating the mineral and OM accretion algorithms, only the algorithm-specific parameters (Tables S1–S2) are adjusted while the parameters related to flow and waves are maintained.

MACES-hydro is validated against observed or benchmark water level, significant wave height, and/or bottom shear stress without calibration. In the experiments to validate MACES-hydro, we configured the model with null mineral and OM accretion algorithms and chose the method of Morris et al. (2012) to calculate aboveground biomass. In the experiments to validate the simulated suspended sediment, we only compared mineral accretion algorithms and used only one OM accretion algorithm at each site that simulates the most realistic aboveground biomass. Because the related observations and benchmark estimates usually cover only a few days, the related validation is only run for a few weeks. For MACES-geomor, because we expect that most of the algorithms can reproduce the observed accretion rates by calibration, our analysis does not focus on validating the individual algorithms explicitly. Instead, we focus on analyzing the uncertainty of mineral and OM accretion algorithms across the 1-D wetland transects, which is important for explaining their divergent predictions in coastal wetland evolution under SLR (Tambroni & Seminara, 2012).

2.4. Model input and evaluation data

We evaluate the model at three representative coastal wetland sites with two located in midlatitude and one located in subtropics: Venice Lagoon, Plum Island Estuary and Hunter Estuary (Table 2). Venice Lagoon is a microtidal wetland with a large central waterbody and extensive intertidal salt marshes. The dominant saltmarsh species include *Limonium serotinum*, *Puccinellia palustris*, *Arthrocnemum fruticosum* and *Spartina maritima*. The long-term mineral and OM accretion rate of the saltmarsh are 3.5 mm yr^{-1} and 132 gC m^{-2} yr^{-1}, respectively (Bellucci et al., 2007; Roner et al., 2016). Plum Island Estuary is a macrotidal wetland with extensive areas of productive, tidal marshes. The dominant saltmarsh species include *Spartina alterniflora* at lower elevations and *Spartina patens* at higher elevations. The long-term mineral accretion rate can be as high as 6.9±0.9 mm yr^{-1} (Wilson et al., 2014) and the long-term OM accretion rate is 69.9±9.4 gC m^{-2} yr^{-1} (Wang et al., 2019). Hunter Estuary is a microtidal wetland with grey mangrove *Avicennia marina* at lower elevations and *Sporobolus virginicus*–*Sarcocornia quinqueflora* mixed saltmarsh at higher elevations. The mineral accretion of mangroves and saltmarsh are 3.66 mm yr^{-1} and 3.37 mm yr^{-1}, respectively (Howe et al., 2009). The OM accretion of mangroves and saltmarsh are 105 gC m^{-2} yr^{-1} and 137 gC m^{-2} yr^{-1}, respectively (Howe et al., 2009).

To simulate the hydrodynamics and eco-geomorphology of coastal wetlands, MACES is driven by the seaward-side water level and SSC and averaged wind speed and air temperature over the coastal transect. We extracted water level and wind conditions from high-frequency (10-minute or 15-minute) measurements for the three sites. The seaward boundary SSC is set based on the high-frequency (15-minute) analytical estimates for Hunter Estuary and as fixed values extracted from the global coastal Database for Impact and Vulnerability Analysis to sea-level rise (DIVA) (Schuerch et al., 2018; Vafeidis et al., 2008) for the other two sites. Daily air

321 temperature was extracted from measurements for Venice Lagoon and Plum Island Estuary and
322 the European Center for Medium-Range Weather Forecasts (ECMWF) Interim reanalysis (ERA-
323 Interim) (Dee & Uppala, 2009) for Hunter Estuary.

324 For each site, we constructed its 1-D transect from high-resolution Digital Elevation
325 Model (DEM) and land cover maps (Hopkinson & Valentine, 2005; Rodríguez et al., 2017;
326 Tambroni & Seminara, 2012; Ye & Pontius, 2016) by: 1) dividing all grid cells into 17 elevation
327 groups spanning from -12.5 m to 16.5 m (some elevation groups can be empty); 2) calculating
328 the average slope and land cover fractions of each elevation group; 3) calculating the transect
329 length of each elevation group based on its slope and elevation range. For the first step, the
330 elevation range of the 17 groups is the largest (i.e., 4 m) near to the land and sea edges and the
331 smallest (i.e., 0.5 m) near to the sea level. For the third step, the slope of a grid cell is calculated
332 by dividing its elevation by its distance to the nearest channel network. The constructed 1-D
333 transects of the three sites are shown in Figure 3.

334 For Venice Lagoon, we use observed water level, SSC and significant wave height and
335 benchmark bottom shear stress estimates from a 2-D hydrodynamic model Wind Wave Tidal
336 Model (WWTM) (Carniello et al., 2011) at two tidal flat stations (1BF: -1.1 masl; 2BF: -2.1 masl)
337 for model evaluation. For Plum Island Estuary, we use observed water level at the channel (-0.73
338 masl) and marsh edge (1.25 masl) of Nelson Island, observed SSC at the channel (-1.45 masl)
339 and marsh interior (1.69 masl) of Law's Point, observed mineral accretion at three saltmarsh
340 stations (LAC: a *Spartina alterniflora*-dominated high saltmarsh with an elevation of 1.1 masl;
341 LPC: a *Spartina patens*-dominated high saltmarsh with an elevation of 1.4 masl; MRS: a
342 *Spartina alterniflora*-dominated high saltmarsh with an elevation of 0.89 masl), and observed
343 aboveground biomass at LAC and MRS for model evaluation. For Hunter Estuary, we use the

benchmark estimates of water level and SSC at four stations (channel: 0.22 mAHD; mangrove edge: 0.05 mAHD; mangrove interior: 0.38 mAHD; saltmarsh edge: 0.65 mAHD) of the wetland for model evaluation. For a specific site, when validating our model over a station, we always choose the grid cell with the closest elevation to the station for comparison. In the model, the total accretion (mm yr^{-1}) is calculated by the Exner equation based on the simulated long-term net sediment deposition (kg m^{-2} yr^{-1}), the simulated long-term net OM deposition (kg C m^{-2} yr^{-1}), sediment bulk density (kg m^{-3}), and sediment porosity. Correspondingly, mineral accretion (mm yr^{-1}) is also estimated using the Exner equation by excluding the contribution of OM deposition.

3. Results

3.1. Simulated hydrodynamics at the three coastal wetland sites

The MACES model can reproduce the observed hydrodynamics at the three coastal wetland sites. The simulated hydrodynamics at Venice Lagoon were validated in the two periods of very different tide and wind conditions: 12/10/2002–12/11/2002 and 4/2/2003–4/4/2003 (Figure 4). Specifically, the spring period in 2003 has the high tide of 64 cm asl and the maximum wind speed of 17.3 m s^{-1} (Figure S2). In contrast, the winter period in 2002 has the much smaller high tide and maximum wind speed: only 38 cm asl and 11.6 m s^{-1}, respectively (Figure S2). The 1-D MACES hydrodynamics module MACES-hydro performs reasonably well in capturing the observed tide and wave dynamics in both periods (Figure 4), with low root-mean-square-errors (RMSE) of simulated water depth and significant wave height at the 1BF and 2BF stations. During the low wind and tide period when observations are available (Figures 4a–4d), the RMSE of simulated water depth at 1BF and 2BF are 5.8 cm and 4.2 cm, respectively, which correspond to only 5% and 2% of the observed mean water depth, and the RMSE of simulated significant wave height at 1BF and 2BF are 4.7 cm and 4.6 cm, respectively, which

correspond to 35% and 19% of the observed mean significant wave height. The model also captures the temporal variability of the bottom shear stress benchmark at 1BF and 2BF during the high tide and wind period, with the RMSE of 0.13 Pa and 0.15 Pa, respectively. It should be noted that as the simulated bottom shear stress is compared to the WWTM model benchmark instead of observations, the evaluation could be marked by substantial uncertainty.

For both periods, the simulated significant wave height mainly followed the wind dynamics (Figure 4). The wind-induced bottom shear stress is also the dominant component of the total bottom shear stress (Figure 4). In the morning of 12/10/2002 when wind speed exceeded 11 m s^{-1}, the simulated significant wave height reached its peak value at the two stations: 22.6 cm and 39.4 cm, respectively. Correspondingly, the simulated bottom shear stress also reached its peak value at the two stations: 0.19 Pa and 0.31 Pa, respectively. On April 3, 2003, when wind speed frequently exceeded 15 m s^{-1}, the simulated significant wave height reached its peak value at the two stations: 31.4 cm and 52.4 cm, respectively. The contribution of the current-induced bottom shear stress to the total bottom shear stress never exceeded 10% in both periods (Figures 4e–4f and 4k–4i), showing that wind action dominates the generation of bottom shear stress. Both the observations and simulations show that 2BF has larger significant wave height values than 1BF. This difference could be explained by the attenuation of wave energy by friction when wave moves toward land as 2BF is deeper and closer to the seaward boundary than 1BF.

The simulated hydrodynamics at Plum Island Estuary were validated in the summer and fall periods of 2017 (7/19–7/22 and 10/7–10/10) when tide and wind conditions were different (Figure 5). In the summer period, the tide level varied substantially, while the wind speed never exceeded 6 m s^{-1} (Figure S3). In contrast, in the fall period, the wind speed sometimes exceeded

8 m s^{-1}, while the tide level varied moderately (Figure S3). For both periods, MACES-hydro captures the observed dynamics of water depth at a river channel station (-0.73 masl) and a saltmarsh station (1.25 masl) reasonably well (Figure 5). The RMSE of the simulated water depth at the river channel station were 9.1 cm and 7.5 cm for the summer and fall periods, respectively. The RMSE of the simulated water depth at the saltmarsh station were 2.2 cm and 1.5 cm for the summer and fall periods, respectively.

The simulated hydrodynamics at Hunter Estuary were validated in the period of 9/28/2004–9/30/2004 for both low-elevation locations where mangrove species reside and high-elevation locations where saltmarsh species reside (Figure 6). MACES-hydro well reproduced the water depth benchmark at four representative locations: a river channel station at an elevation of -0.22 mAHD (Figure 6a), a mangrove-dominated station at an elevation of 0.05 mAHD (Figure 6b), a mangrove-dominated interior station at an elevation of 0.38 mAHD (Figure 6c), and a saltmarsh-dominated station at an elevation of 0.65 mAHD (Figure 6d). The RMSE of the simulated water depth at the four stations were 4.6 cm, 5.4 cm, 2.7 cm and 0.4 cm, respectively.

Importantly, as shown by our simulations, the water level across a coastal wetland transect is far from being spatially uniform if the seaward boundary is not extremely close to the shoreline. For instance, at Venice Lagoon and Plum Island Estuary where the distance from the seaward boundary to the shoreline is more than 18 km and 0.7 km, respectively, the water level peaks in the wetland interiors clearly lagged those at the boundary (Figures 4–5), showing the effect of bed roughness on water flow. In contrast, at Hunter Estuary where the seaward boundary is very close to the shoreline (only 20 m in distance), the difference between the simulated water level and the boundary condition is negligible (Figure 6).

3.2. Simulated suspended sediment dynamics at the three coastal wetland sites

413 The MACES model can also capture the dynamics of suspended sediment at the three
414 coastal wetland sites reasonably well when appropriate mineral accretion algorithms are selected.
415 For Venice Lagoon, the observed SSC at 1BF during the low wind and tide period ranged from
416 7.3 mg l^{-1} to 92.0 mg l^{-1} (Figure 7), with one larger peak value occurring on the windy morning
417 of 12/10/2002 and one smaller peak value occurring on the morning of 12/11/2002 (Figure 4).
418 Three out of the seven mineral accretion algorithms, including M12, F07 and DA07, can
419 reproduce the observed two SSC peaks (Figure 7). Among the algorithms, the F07 algorithm has
420 the lowest RMSE of 12.0 mg l^{-1} as well as the lowest normalized RMSE (NRMSE) of 0.45. But
421 even the three best performing algorithms overestimated SSC at the mid-day of 12/10/2002. A
422 possible reason is that the model does not reproduce the rapid decrease of wave energy after the
423 windy morning on 12/10/2002. The simulated SSC by F06, T03 and KM12 is almost constant
424 because these algorithms do not represent sediment resuspension (Section 2.1, 2.2 and 2.3 of
425 Text S1) and there is limited sediment deposition at 1BF. As a result, the SSC is almost entirely
426 determined by the seaward boundary (9.4 mg l^{-1}) which was extracted from the DIVA database.
427 It should be noted that the dynamics of suspended sediment in the coast is notoriously difficult to
428 model (Le Hir et al., 2007; Temmerman et al., 2003). Thus, the performance achieved by our 1-
429 D model is satisfactory.
430 For Plum Island Estuary, the MACES model reproduces the temporal variability of SSC
431 at a river channel station (-1.45 masl) and the decrease of SSC from the river channel to a
432 saltmarsh station (1.69 masl) in the summer period of 2017 reasonably well (Figure 8). Because
433 the river channel station is close to the model boundary (Figure 3), its suspended sediment
434 dynamics is strongly regulated by the SSC boundary condition (Figure S3) and the difference
435 between different algorithms is mainly caused by the simulated sediment deposition rather than

436 the simulated sediment resuspension. Among the algorithms, the M12 algorithm has the lowest
437 RMSE of 7.4 mg l^{-1} as well as the lowest NRMSE of 0.57 at the river channel station. There are
438 several SSC peaks at the river channel that our model fails to capture (Figure 8), which could be
439 attributed to the uncertainty of the boundary condition. For the saltmarsh station, the
440 performance of different algorithms is similar, implying that all the algorithms predicted
441 reasonable sediment deposition over the saltmarsh planform.

442 The MACES model also captures the temporal variability of SSC along the elevation
443 gradient of Hunter Estuary from the river channel, the mangrove edge, the mangrove interior to
444 the saltmarsh edge (Figure 9). Because the river channel station in this case is even closer to the
445 model boundary than in Plum Island Estuary (Figure 3), the dynamics of suspended sediment is
446 strongly regulated by the boundary condition (Figure S4) before being fully deposited at the
447 saltmarsh edge. The four more complex algorithms, including M12, F07, VDK05 and DA07,
448 outperform the three simpler algorithms (i.e., F06, T03 and KM12). Overall, the M12 algorithm
449 has the best performance at the four stations: the RMSE of 1.6 mg l^{-1} at the river channel, 0.9 mg
450 l^{-1} at the mangrove edge, 2.8 mg l^{-1} at the mangrove interior and 0.4 mg l^{-1} at the saltmarsh edge,
451 respectively (we removed data points in the comparison when the simulated water depth was
452 zero). This result may indicate that more sophisticated mineral accretion algorithms are needed
453 to reasonably represent sediment deposition at this wetland site. But we should note that these
454 algorithms seem to underestimate sediment deposition in the mangrove wetland area. It is
455 possibly because mineral accretion algorithms were usually developed based on the saltmarsh
456 studies and are less applicable to mangrove wetlands.

457 **3.3. Simulated mineral and OM accretion at the three coastal wetland sites**

458 Once carefully calibrated, most of the MACES mineral and OM accretion algorithms can
459 reproduce the observed long-term mineral and OM accretion rates at the three coastal wetland
460 sites, especially when the accretion rates are only measured at single locations. But different
461 algorithms demonstrate remarkable variations in the simulated mineral and OM accretion along
462 the elevation gradient. Moreover, our ensemble simulations show that the variations of the
463 simulated mineral and OM accretion along the elevation gradient differ substantially among the
464 coastal wetland sites.

465 For Venice Lagoon, all of the seven mineral accretion and four OM accretion algorithms
466 can predict the observed long-term mineral accretion rate of 3.54 mm yr^{-1} and the observed long-
467 term OM accretion rate of 132 gC m^{-2} yr^{-1}, respectively, at the observation station that is about
468 0.2 km from the marsh shore edge (Figure 10). The good model performance does not rely on
469 which OM accretion or mineral accretion algorithm is combined. For example, for the F06
470 mineral accretion algorithm, its combination with the M12 OM accretion algorithm performs
471 comparably to that with the DA07 OM accretion algorithm. Despite the convergence of different
472 algorithms at the observation station, the simulated summer aboveground biomass, OM accretion
473 and mineral accretion along the elevation gradient differ substantially among the algorithms
474 (Figure 10). For the summer aboveground biomass at the saltmarsh, the M12 algorithm predicts
475 an increasing trend with elevation, while the other three algorithms predict slight decreases
476 (Figure 10a). Also, the marsh aboveground biomass simulated by M12 is much higher than those
477 by the other algorithms (Figure 10a), even though the estimates are all within the reported range
478 of 1–3 kg m^{-2} (Tambroni & Seminara, 2012). Driven by the change of aboveground biomass, the
479 M12 algorithm predicts an increase of OM accretion with elevation and the algorithms of DA07
480 and K16 predicts a decrease (Figure 10b). However, KM12 predicts an increase of OM accretion

with elevation despite the decrease of simulated aboveground biomass. It is because KM12 simulates a much larger increase of the root:shoot quotient along the elevation gradient. For mineral accretion, the algorithms of F06 and KM12 predict a moderate increase with elevation, the algorithms of F07 and VDK05 predict its moderate decrease, and the other algorithms predict its rapid decrease (Figure 10c). As a result, the simulated mineral accretion differs remarkably at both the marsh shore edge and the marsh-upland interface. For example, at the saltmarsh edge, the estimate by T03 is over 6 mm yr^{-1} but that by F06 is less than 4 mm yr^{-1}. In contrast, at the 1.5 km to the edge, the estimate by T03 falls close to zero but that by F06 is over 4 mm yr^{-1}. Importantly, our model can provide the multi-algorithm ensemble estimate of mineral and OM accretion over the saltmarsh, which shows that the total accretion gradually decreases along the elevation gradient with the importance of OM accretion moderately increasing (Figure 10d). However, mineral accretion is almost always the dominant source over the saltmarsh platform. It should be noted that this more robust signal would be difficult to discern using single-algorithm simulations.

For Plum Island Estuary, when comparing with more spatiotemporally resolved validation data, some mineral and OM accretion algorithms show clearly better performance than the others. For instance, while all the OM accretion algorithms provide satisfactory simulations of the summer aboveground biomass distribution along the elevation gradient, M12 seems to capture the higher saltmarsh biomass at the edge more reasonably (Figure 11a). Also, the algorithms of DA07 and KM12 can simulate the seasonality of the saltmarsh biomass at the high marsh station LAC (1.1 masl), while the algorithms of M12 and K16 cannot simulate any seasonality (Figure 11c). All the OM accretion algorithms successfully predict the observed long-term OM accretion rate (69.9±9.4 gC m^{-2} yr^{-1}) within the elevation range of 0–1.5 masl

(Figure S3). Furthermore, we find that all the mineral accretion algorithms except F06 and KM12 can reproduce the observed long-term mineral accretion rates at the *Spartina alterniflora*-dominated low marsh station MRS (6.9±0.9 mm yr^{-1}), the *Spartina alterniflora*-dominated high saltmarsh station LAC (5.3±0.1 mm yr^{-1}) and the *Spartina patens*-dominated high saltmarsh station LPC (2.3±0.1 mm yr^{-1}) (Figure 11d), which shows the decline of mineral accretion along the elevation gradient. It implies that the use of F06 and KM12 at Plum Island Estuary may lead to biased predictions of the saltmarsh's resilience to SLR. Like Venice Lagoon, the multi-algorithm ensemble estimate indicates that the total accretion gradually decreases along the elevation gradient with the importance of OM accretion increasing (Figure 11e). However, different from Venice Lagoon, OM accretion can dominate the total accretion at some high marsh areas of Plum Island Estuary. This is possibly because the platform of Plum Island Estuary has a much larger elevation gradient than that of Venice Lagoon (Figure 3) that impairs the landward transport of suspended sediment.

For Hunter Estuary, different mineral and OM accretion algorithms can also reproduce the observed long-term mineral accretion rate (3.66 mm yr^{-1}) and OM accretion rate (105 gC m^{-2} yr^{-1}) at the mangrove-dominated station (0.56 mAHD) after calibration (Figure 12). All the four OM accretion algorithms predict the decrease of aboveground biomass along the elevation gradient and from the mangrove-dominated area at low elevations to the saltmarsh-dominated area at high elevation (Figure 12a). The simulated aboveground biomass is consistent with the reported values that are 1000 g m^{-2} and 900 g m^{-2} for mangrove and saltmarsh, respectively (Rodríguez et al., 2017). Driven by aboveground biomass, the simulated OM accretion by M12, DA07 and K16 decreases along the elevation gradient (Figure 12b). The simulated OM accretion by KM12 increases with elevation despite the negative relationship between aboveground

biomass and elevation. As discussed for Venice Lagoon, it is caused by a much larger increase of the root:shoot quotient along the elevation gradient parameterized in KM12. The discontinuity of the simulated OM accretion at the mangrove-saltmarsh boundary by the DA07 is because the root:shoot quotient of saltmarsh species in the DA07 is set to be higher than that of mangrove species (Kakeh et al., 2016), but these quotient ratios may also vary depending on the hydrodynamic conditions and salinity gradient (Sandi et al., 2021). In Hunter Estuary, the simulated mineral accretion on the platform shows two spatial patterns: the nearly constant rate by the algorithms of F06, T03 and KM12 and the decline rate by the other algorithms (Figure 12c). Notably, in the latter group, the simulated mineral accretion rate at the wetland shore edge is well above 10 mm yr^{-1}, which is much higher than that at Venice Lagoon and Plum Island Estuary, but the variation of accretion across the section follows a similar general as other of recent eco-geomorphic simulations in the Hunter Estuary using a simplified 2-D domain (Breda et al. 2021). The multi-algorithm ensemble estimates show that mineral accretion dominates the total accretion in all the areas of the platform except the area close to the wetland-upland boundary (Figure 12d). As explained for Plum Island Estuary, it is mainly because the large platform slope at Hunter Estuary impairs the landward transport of suspended sediment (Figure 3).

4. Discussion

4.1. Algorithm-level uncertainties of modeling coastal wetland eco-geomorphology

It is not surprising that significant algorithm-level uncertainties exist in the modeled eco-geomorphology at the three coastal wetland sites. However, our study shows that a multi-algorithm ensemble simulation approach may provide more robust signals about the evolution of coastal wetlands in different environments and thus help reduce the prediction uncertainty. For

example, the multi-algorithm ensembles reveal that it is critical to represent OM accretion in the coastal wetland eco-geomorphology models to realistically predict coastal wetland resilience under future SLR. This is because while OM accretion may only account for 10% of the total accretion at low-elevation saltmarsh or mangrove, its contribution in the higher elevation areas is much larger and even surpasses the contribution from mineral accretion. As a result, ignoring OM accretion would cause a significant underestimation of coastal wetland survival.

To reduce the algorithm-level uncertainty in the simulation of coastal wetland evolution, it is also important to constrain mineral and OM accretion algorithms using observations from at least two locations at different elevations of a coastal wetland site. For example, if mineral accretion was only observed at the *Spartina patens*-dominated high saltmarsh station LPC and the algorithm of F06 or KM12 was chosen for modeling, the prediction on the resilience of coastal wetlands to SLR would be severely biased. Thus, new observations should be prioritized to capture the elevation and vegetation gradients of mineral and OM accretion. Although we focus on the model structural uncertainty and thus carefully calibrate the model parameters for each algorithm in this study, the use of multi-location observations at different elevations can also help reduce the parameter uncertainty of eco-geomorphology modeling. For instance, for Plum Island Estuary, if only the LPC station is benchmarked, even those good algorithms (i.e., T03, M12, F07, VDK05 and DA07), albeit reproducing the decline of mineral accretion with elevation, would produce widespread estimates of mineral accretion at the low-marsh station MRS.

Although the existence of substantial algorithm-level uncertainties in coastal wetland eco-geomorphology models is expected, due to the variations of coastal wetland characteristics, such as tidal range, SSC, topography, and vegetation species, they cannot be fully learned by

analyzing the mathematical formulations only. Instead, these uncertainties must be carefully evaluated using a multi-algorithm approach like MACES. For example, as the mineral accretion algorithms of F06 and KM12 use spatially constant SSC to derive sediment deposition, it would be expected that the estimated mineral accretion by these two algorithms is uniform over coastal wetland platforms. However, with the simulated bottom shear stress declining with the water depth along the elevation gradient, the simulated force to resuspend sediment decreases in higher elevation wetland and correspondingly sediment deposition is simulated to increase along the elevation gradient. Furthermore, this effect varies among the coastal wetland sites due to the difference in tidal range, topography and vegetation species (Figures 10–12). Similarly, while it is expected that the simulated mineral accretion by M12, F07, VDK05 and DA07 would decrease with elevation because the modeled SSC in the interior areas decreases due to deposition and sediment resuspension is weak over the vegetated platform, it is still difficult to discern which algorithm simulates the strongest declining effect without testing the algorithms in a united hydrodynamics model.

4.2. Modeling coastal wetland eco-geomorphology in diverse environments

Coastal wetlands are an important ecosystem type spanning broad geographic regions, from tropical and subtropical mangroves, midlatitude saltmarshes to arctic coastal tundra (Keddy, 2000). Through the application of a multi-algorithm model framework developed in this study, we show that the uncertainties of coastal wetland eco-geomorphology models should be evaluated for coastal wetlands in diverse environments. Previous studies that rely on the knowledge of a single type of coastal wetlands for the prediction of large-scale coastal wetland response to SLR may lead to unreliable conclusions. For example, while Venice Lagoon and Plum Island Estuary are both saltmarshes, due to the difference in environments, there are

substantial distinctions on the simulated mineral and OM accretion at the two sites, including the much more important role of OM accretion to the rise of saltmarsh bed against SLR at Plum Island Estuary. Correspondingly, a multi-algorithm approach that include diverse eco-geomorphology algorithms can be more capable to predict large-scale coastal wetland evolution. As demonstrated in the study, MACES includes the mineral and OM accretion algorithms that can be applied to the most common plant species of coastal wetlands (Crase et al., 2013; Day Jr et al., 1999; Kirwan & Mudd, 2012; Liu et al., 2020; Morris et al., 2002; Mudd et al., 2010; Temmerman et al., 2003b): *Spartina alterniflora*, *Spartina patens*, *Puccinellia palustris*, *Spartina maritima* and *Avicennia marina*. Particularly, very few eco-geomorphology modeling studies have included both saltmarsh and mangrove. These algorithms can also be applied to different tidal ranges (microtidal and macrotidal) and climate (Mediterranean climate, humid continental climate and humid subtropical climate). Furthermore, although we have not validated the algorithms of wave-action erosion and landward migration in this study, they have been implemented in the MACES model. The inclusion of these processes in the multi-algorithm approach would further extend the model's applicability to diverse environments.

As the algorithm-level uncertainties of eco-geomorphology models are site dependent, this multi-algorithm model framework can also be used to select appropriate eco-geomorphology algorithms for specific coastal wetland environment. For example, our simulation indicates that it is better to avoid the use of F06 and KM12 to predict the evolution of coastal wetlands in an environment similar to Plum Island Estuary but these two mineral accretion algorithms can still be useful for coastal wetlands like Venice Lagoon. To extend this algorithm selection strategy to the global scale, it would need the related observations across diverse environments. Currently, there have already been many published datasets of mineral and OM accretion from coastal

wetlands across broad regions (Breithaupt et al., 2012; Chmura et al., 2003; Crosby et al., 2016; Lovelock et al., 2015; Parkinson et al., 2017). The next step would be to identify and survey geographic and ecological factors that are crucial for the classification of coastal wetlands. Nevertheless, the development of this multi-algorithm coastal wetland eco-geomorphology model will facilitate the reduction of algorithm-level uncertainties in global applications.

4.3. Limitations and future work

To prioritize computational efficiency and the representation of suspended sediment dynamics, we have chosen to model coastal wetland eco-geomorphology on a simplified 1-D coastal transect. As a result, the MACES model cannot resolve the detailed spatial heterogeneity of coastal wetland dynamics that are needed for decision making and damage mitigation. For instance, while the model can assess the overall wetland vulnerability under SLR, it cannot be used to locate specific areas for remedy. Additionally, because the simulated variables are not linked with specific locations, the impact of SLR and other climate extremes on the ecosystem services of coastal wetlands cannot be reasonably evaluated by the current MACES framework. A possible solution is to use the emerging machine learning techniques to downscale low-fidelity high-efficiency hydrodynamics models to emulate the high-fidelity low-efficiency hydrodynamics models (Feng et al., 2023; Fraehr et al., 2023).

Although we intend to drive all the mineral and OM accretion algorithms with the same hydrodynamic conditions, particularly water level and SSC, due to the impact of vegetation on the transect surface roughness (Eq. S1.3), the simulated hydrodynamics would be changed by the choice of mineral and OM accretion algorithms. As a result, the simulated differences of mineral and OM accretion may not be fully caused by the algorithm-level uncertainties.

Another limitation of the model is the very simplified representation of the biological and biogeochemical processes in MACES that could limit the prediction accuracy of OM accretion. Despite the importance of macroclimatic drivers (particularly air temperature) to the evolution of coastal wetlands under climate change (Osland et al., 2016), the related effects are either neglected or only simply parameterized in the MACES algorithms (D'Alpaos et al., 2007; Kakeh et al., 2016; Kirwan & Mudd, 2012; Morris et al., 2012), which would cause biased estimates of sediment deposition, OM deposition and coastal wetlands resilience (Schoutens et al., 2019). In the future, it is thus necessary to adopt some advanced developments of vegetation dynamics and biogeochemistry from more complex land surface models (Oleson et al., 2013). In addition, it will be valuable to extend the framework to the other two processes (Table 1), including landward migration and wave-action erosion, which are also important for coastal wetland resilience (Mariotti & Fagherazzi, 2010; Schuerch et al., 2018) but have not been evaluated due to data limitation.

Our future work will also include the application of the model framework to the global scale. One challenge is to delineate 1-D coastal wetland transects for different regions of the world which needs high-quality high-resolution digital terrain and land cover data. Some recently published datasets, such as 30-m resolution high-quality Forest And Buildings removed Copernicus Digital Elevation Model (FABDEM) (Hawker et al., 2022) and the high-resolution global distribution map of mangroves and saltmarshes compiled by US Geological Survey and the World Conservation and Monitoring Centre (http://data.unep-wcmc.org/), may facilitate the model's global applications.

5. Conclusion

We developed a multi-algorithm model framework MACES to evaluate the algorithm-level uncertainties of mineral and OM accretion modeling based on consistent hydrodynamic conditions. This model framework was validated for hydrodynamics and mineral and OM accretion at three representative coastal wetland sites of diverse environments: the microtidal saltmarsh site of Venice Lagoon, the macrotidal saltmarsh site of Plum Island Estuary, and the microtidal mangrove and saltmarsh mixed site of Hunter Estuary. The MACES model can reproduce the observed dynamics of water depth, wave, and bottom shear stress and also the observed long-term mineral and OM accretion. As expected, our approach shows that there are significant algorithm-level uncertainties in coastal wetland eco-geomorphology models, which can lead to divergent estimates of the coastal wetland vulnerability under SLR. In contrast, multi-algorithm ensemble estimates from MACES can provide more robust signals on the evolution of coastal wetlands. Additionally, our study indicates that more observations of mineral and OM accretion along the elevation gradient of coastal wetlands and the evaluation of the coastal wetland models at different sites of diverse environments can also help reduce the model uncertainty. The MACES framework provides a useful tool to realistically predict the fate of coastal wetlands under climate change at large scales.

Open Research

The MACES source code can be freely downloaded from Tan (2023) and will be routinely updated at https://github.com/tanzeli1982/MACES. The data used in this study are publicly available at Tan et al. (2023).

Acknowledgements: We appreciate Dr. Maarten Kleinhans and one anonymous reviewer for their valuable comments. The research is supported by the U.S. Department of Energy, Office of Science, Office of Biological and Environmental Research as part of the multi-program, collaborative Integrated Coastal Modeling (ICoM) project. It is also partly supported by PREMIS Initiative at Pacific Northwest National Laboratory (PNNL) under the Laboratory Directed Research and Development Program. PNNL is operated for DOE by Battelle Memorial Institute, United States under contract DE-AC05-76RL01830. The authors wish to thank the Ministero delle Infrastrutture e dei Trasporti, Magistrato alle Acque di Venezia, through its concessionary Consorzio Venezia Nuova for the field data collected in the Venice lagoon. Data sets of Plum Island Estuary were provided by the Plum Island Ecosystems LTER, with the support by the National Science Foundation under Grants #OCE-9726921, OCE-0423565, OCE-1058747, OCE-1238212, OCE-1637630.

References

Aburto-Oropeza, O., Ezcurra, E., Danemann, G., Valdez, V., Murray, J., & Sala, E. (2008). Mangroves in the Gulf of California increase fishery yields. *Proceedings of the National Academy of Sciences*, **105**, 10456–10459.

Bellucci, L. G., Frignani, M., Cochran, J. K., Albertazzi, S., Zaggia, L., Cecconi, G., & Hopkins, H. (2007). ^{210}Pb and ^{137}Cs as chronometers for salt marsh accretion in the Venice Lagoon–links to flooding frequency and climate change. *Journal of Environmental Radioactivity*, **97**, 85–102.

Blum, M. D., & Roberts, H. H. (2009). Drowning of the Mississippi Delta due to insufficient sediment supply and global sea-level rise. *Nature Geoscience*, **2**, 488–491.

Breda, A., Saco, P. M., Sandi, S. G., Saintilan, N., Riccardi, G., & Rodríguez, J. F. (2021). Accretion, retreat and transgression of coastal wetlands experiencing sea-level rise. *Hydrology and Earth System Sciences*, *25*, 769–786.

Breithaupt, J. L., Smoak, J. M., Smith, T. J., Sanders, C. J., & Hoare, A. (2012). Organic carbon burial rates in mangrove sediments: Strengthening the global budget. *Global Biogeochemical Cycles*, **26**, GB3011.

713 Burden, R. L., Faires, J. D., & Reynolds, A. C. (1978). *Numerical Analysis* (pp. 254). Boston:
714 Prindle, Weber and Schmidt Inc.

715 Cahoon, D. R., Hensel, P. F., Spencer, T., Reed, D. J., McKee, K. L., & Saintilan, N. (2006).
716 Coastal wetland vulnerability to relative sea-level rise: wetland elevation trends and process
717 controls, in *Wetlands and Natural Resource Management: Ecological Studies*, vol. 190, edited
718 by J. T. A. Verhoeven et al., pp. 271–292, doi:10.1007/978-3-540-33187-2_12, Springer, Berlin.

719 Cahoon, D. R., McKee, K. L., & Morris, J. T. (2021). How plants influence resilience of salt
720 marsh and mangrove wetlands to sea-level rise. *Estuaries and Coasts*, *44*, 883–898.

721 Cao, Z., Zhang, Y., Wolfram, P. J., Brus, S. R., Rowland, J. C., Xu, C., ... & Petersen, M. R.
722 (2021). Effects of different vegetation drag parameterizations on the tidal propagation in coastal
723 marshlands. *Journal of Hydrology*, **603**, 126775.

724 Carniello, L., Defina, A., Fagherazzi, S., & D'Alpaos, L. (2005). A combined wind wave–tidal
725 model for the Venice lagoon, Italy. *Journal of Geophysical Research: Earth Surface*, **110**,
726 F04007.

727 Carniello, L., D'Alpaos, A., & Defina, A. (2011). Modeling wind waves and tidal flows in
728 shallow micro-tidal basins. *Estuarine, Coastal and Shelf Science*, **92**, 263–276.

729 Carniello, L., Defina, A., & D'Alpaos, L. (2012). Modeling sand-mud transport induced by tidal
730 currents and wind waves in shallow microtidal basins: Application to the Venice Lagoon (Italy).
731 *Estuarine, Coastal and Shelf Science*, **102**, 105–115.

732 Chmura, G. L., Anisfeld, S. C., Cahoon, D. R., & Lynch, J. C. (2003). Global carbon
733 sequestration in tidal, saline wetland soils. *Global Biogeochemical Cycles*, **17**, 1111.

734 Coleman, D., & Kirwan, M. (2020). PIE LTER suspended sediments at Law's Point, West Creek,
735 a tidal marsh and creek off the Rowley River, Rowley, MA, during 2016-2017. Environmental
736 Data Initiative.

737 Craft, C., Clough, J., Ehman, J., Joye, S., Park, R., Pennings, S., ... & Machmuller, M. (2009).
738 Forecasting the effects of accelerated sea-level rise on tidal marsh ecosystem services. *Frontiers*
739 *in Ecology and the Environment*, **7**, 73**–**78.

740 Crase, B., Liedloff, A., Vesk, P. A., Burgman, M. A., & Wintle, B. A. (2013). Hydroperiod is the
741 main driver of the spatial pattern of dominance in mangrove communities. *Global Ecology and*
742 *Biogeography*, **22**, 806–817.

743 Crosby, S. C., Sax, D. F., Palmer, M. E., Booth, H. S., Deegan, L. A., Bertness, M. D., & Leslie,
744 H. M. (2016). Salt marsh persistence is threatened by predicted sea-level rise. *Estuarine, Coastal*
745 *and Shelf Science*, **181**, 93–99.

D'Alpaos, A., Lanzoni, S., Marani, M., & Rinaldo, A. (2007). Landscape evolution in tidal embayments: Modeling the interplay of erosion, sedimentation, and vegetation dynamics. *Journal of Geophysical Research: Earth Surface*, **112**, F01008.

D'Alpaos, A., Carniello, L., & Mudd, S. M. (2011). Dynamic response of marshes to perturbations in suspended sediment concentrations and rates of relative sea level rise. *Journal of Geophysical Research: Earth Surface*, **116**, F04020.

Day Jr, J. W., Rybczyk, J., Scarton, F., Rismondo, A., Are, D., & Cecconi, G. (1999). Soil accretionary dynamics, sea-level rise and the survival of wetlands in Venice Lagoon: a field and modelling approach. *Estuarine, Coastal and Shelf Science*, **49**, 607–628.

Dee, D. P., & Uppala, S. (2009). Variational bias correction of satellite radiance data in the ERA-Interim reanalysis. *Quarterly Journal of the Royal Meteorological Society*, **135**, 1830–1841.

Deegan, L. A., Johnson, D. S., Warren, R. S., Peterson, B. J., Fleeger, J. W., Fagherazzi, S., & Wollheim, W. M. (2012). Coastal eutrophication as a driver of salt marsh loss. *Nature*, **490**, 388–392.

Deltares (2022). D-Morphology, 1D/2D/3D user manual, Version 2023.

Doherty, J., Brebber, L., & Whyte, P. (1994). *PEST: Model-independent parameter estimation* (Vol. 122). Corinda, Australia: Watermark Computing.

Donatelli, M., Bregaglio, S., Confalonieri, R., De Mascellis, R., & Acutis, M. (2014). A generic framework for evaluating hybrid models by reuse and composition–A case study on soil temperature simulation. *Environmental Modelling & Software*, **62**, 478–486.

Fagherazzi, S., Palermo, C., Rulli, M. C., Carniello, L., & Defina, A. (2007). Wind waves in shallow microtidal basins and the dynamic equilibrium of tidal flats. *Journal of Geophysical Research: Earth Surface*, **112**, F02024.

Fagherazzi, S., Kirwan, M. L., Mudd, S. M., Guntenspergen, G. R., Temmerman, S., D'Alpaos, A., ... & Clough, J. (2012). Numerical models of salt marsh evolution: Ecological, geomorphic, and climatic factors. *Reviews of Geophysics*, **50**, RG1002.

Feng, D., Tan, Z., Engwirda, D., Liao, C., Xu, D., Bisht, G., ... & Leung, L. R. (2022). Investigating coastal backwater effects and flooding in the coastal zone using a global river transport model on an unstructured mesh. *Hydrology and Earth System Sciences*, **26**, 5473–5491.

Feng, D., Tan, Z., & He, Q. (2023). Physics-informed neural networks of the Saint-Venant equations for downscaling a large-scale river model. *Water Resources Research*, **59**, e2022WR033168.

Fisher, R. A., & Koven, C. D. (2020). Perspectives on the future of land surface models and the challenges of representing complex terrestrial systems. *Journal of Advances in Modeling Earth Systems*, **12**, e2018MS001453.

Fraehr, N., Wang, Q. J., Wu, W., & Nathan, R. (2023). Development of a fast and accurate hybrid model for floodplain inundation simulations. *Water Resources Research*, **59**, e2022WR033836.

French, J. (2006). Tidal marsh sedimentation and resilience to environmental change: exploratory modelling of tidal, sea-level and sediment supply forcing in predominantly allochthonous systems. *Marine Geology*, **235**, 119–136.

Giblin, A. (2018). Year 2017, PIE LTER wind sensor data, 15 minute intervals, from the Ipswich Bay Yacht Club pier located in Ipswich, MA Environmental Data Initiative.

Giblin, A. (2019). PIE LTER marsh water table height, logging data from the Nelson Island Spartina marsh site, Rowley, MA for May-October 2017. Environmental Data Initiative.

Guseva, S., Bleninger, T., Jöhnk, K., Polli, B. A., Tan, Z., Thiery, W., ... & Stepanenko, V. (2020). Multimodel simulation of vertical gas transfer in a temperate lake. *Hydrology and Earth System Sciences*, **24**, 697–715.

Hawker, L., Uhe, P., Paulo, L., Sosa, J., Savage, J., Sampson, C., & Neal, J. (2022). A 30 m global map of elevation with forests and buildings removed. *Environmental Research Letters*, **17**, 024016.

Hopkinson, C., & Valentine, V. (2005). PIE LTER 2005 Digital elevation model for the Plum Island Sound estuary, Massachusetts, filtered_grd, last filtered grid - Raster Environmental Data Initiative.

Howe, A. J., Rodríguez, J. F., & Saco, P. M. (2009). Surface evolution and carbon sequestration in disturbed and undisturbed wetland soils of the Hunter estuary, southeast Australia. *Estuarine, Coastal and Shelf Science*, **84**, 75–83.

Howes, N. C., FitzGerald, D. M., Hughes, Z. J., Georgiou, I. Y., Kulp, M. A., Miner, M. D., ... & Barras, J. A. (2010). Hurricane-induced failure of low salinity wetlands. *Proceedings of the National Academy of Sciences*, **107**, 14014–14019.

Huntzinger, D. N., Schwalm, C., Michalak, A. M., Schaefer, K., King, A. W., Wei, Y., ... & Berthier, G. (2013). The North American Carbon Program Multi-Scale Synthesis and Terrestrial Model Intercomparison Project – Part 1: Overview and experimental design. *Geoscientific Model Development*, **6**, 2121–2133.

Jin, Z., Zhuang, Q., Tan, Z., Dukes, J. S., Zheng, B., & Melillo, J. M. (2016). Do maize models capture the impacts of heat and drought stresses on yield? Using algorithm ensembles to identify successful approaches. *Global Change Biology*, **22**, 3112–3126.

Kakeh, N., Coco, G., & Marani, M. (2016). On the morphodynamic stability of intertidal environments and the role of vegetation. *Advances in Water Resources*, **93**, 303–314.

Keddy, P. A. (2000). *Wetland ecology: principles and conservation*. Cambridge, UK: Cambridge University Press.

Kirwan, M. L., Guntenspergen, G. R., d'Alpaos, A., Morris, J. T., Mudd, S. M., & Temmerman, S. (2010). Limits on the adaptability of coastal marshes to rising sea level. *Geophysical Research Letters*, **37**, L23401.

Kirwan, M. L., & Mudd, S. M. (2012). Response of salt-marsh carbon accumulation to climate change. *Nature*, **489**, 550–553.

Kirwan, M. L., & Megonigal, J. P. (2013). Tidal wetland stability in the face of human impacts and sea-level rise. *Nature*, **504**, 53–60.

Kirwan, M. L., Temmerman, S., Skeehan, E. E., Guntenspergen, G. R., & Fagherazzi, S. (2016). Overestimation of marsh vulnerability to sea level rise. *Nature Climate Change*, **6**, 253–260.

Kurganov, A., & Levy, D. (2002). Central-upwind schemes for the Saint-Venant system. *ESAIM: Mathematical Modelling and Numerical Analysis*, **36**, 397–425.

Langston, A. K., Durán Vinent, O., Herbert, E. R., & Kirwan, M. L. (2020). Modeling long-term salt marsh response to sea level rise in the sediment-deficient Plum Island Estuary, MA. *Limnology and Oceanography*, **65**, 2142–2157.

Le Hir, P., Monbet, Y., & Orvain, F. (2007). Sediment erodability in sediment transport modelling: Can we account for biota effects?. *Continental Shelf Research*, **27**, 1116-1142.

Leonardi, N., Ganju, N. K., & Fagherazzi, S. (2016). A linear relationship between wave power and erosion determines salt-marsh resilience to violent storms and hurricanes. *Proceedings of the National Academy of Sciences*, **113**, 64–68.

Liang, Q., & Marche, F. (2009). Numerical resolution of well-balanced shallow water equations with complex source terms. *Advances in water resources*, **32**, 873–884.

Liao, C., Zhuang, Q., Leung, L. R., & Guo, L. (2019). Quantifying dissolved organic carbon dynamics using a three‐dimensional terrestrial ecosystem model at high spatial‐temporal resolutions. *Journal of Advances in Modeling Earth Systems*, **11**, 4489**–** 4512.

Liu, W., Chen, X., Strong, D. R., Pennings, S. C., Kirwan, M. L., Chen, X., & Zhang, Y. (2020). Climate and geographic adaptation drive latitudinal clines in biomass of a widespread saltmarsh plant in its native and introduced ranges. *Limnology and Oceanography*, **65**, 1399–1409.

Lovelock, C. E., Cahoon, D. R., Friess, D. A., Guntenspergen, G. R., Krauss, K. W., Reef, R., ... & Saintilan, N. (2015). The vulnerability of Indo-Pacific mangrove forests to sea-level rise. *Nature*, **526**, 559–563.

Maan, D. C., Van Prooijen, B. C., Wang, Z. B., & De Vriend, H. J. (2015). Do intertidal flats ever reach equilibrium?. *Journal of Geophysical Research: Earth Surface*, **120**, 2406–2436.

Maan, D. C., van Prooijen, B. C., & Wang, Z. B. (2019). Progradation speed of tide-dominated tidal flats decreases stronger than linearly with decreasing sediment availability and linearly with sea level rise. *Geophysical Research Letters*, **46**, 262–271.

852 Marani, M., D'Alpaos, A., Lanzoni, S., Carniello, L., & Rinaldo, A. (2007). Biologically-
853 controlled multiple equilibria of tidal landforms and the fate of the Venice lagoon. *Geophysical*
854 *Research Letters*, **34**, L11402.

855 Macreadie, P. I., Anton, A., Raven, J. A., Beaumont, N., Connolly, R. M., Friess, D. A., ... &
856 Lovelock, C. E. (2019). The future of Blue Carbon science. *Nature Communications*, **10**, 3998.

857 Mariotti, G., & Fagherazzi, S. (2010). A numerical model for the coupled long-term evolution of
858 salt marshes and tidal flats. *Journal of Geophysical Research: Earth Surface*, **115**, F01004.

859 Mcleod, E., Poulter, B., Hinkel, J., Reyes, E., & Salm, R. (2010). Sea-level rise impact models
860 and environmental conservation: A review of models and their applications. *Ocean & Coastal*
861 *Management*, **53**, 507–517.

862 Morris, J. T., Sundareshwar, P. V., Nietch, C. T., Kjerfve, B., & Cahoon, D. R. (2002).
863 Responses of coastal wetlands to rising sea level. *Ecology*, **83**, 2869–2877.

864 Morris, J., & Sundberg, K. (2006). Change in marsh surface elevation measured with a Surface
865 Elevation Table (SET) at control plots in a *Spartina alterniflora*-dominated salt marsh at Law's
866 Point, Rowley River, Plum Island Ecosystem LTER, MA. Environmental Data Initiative.

867 Morris, J. T., Edwards, J., Crooks, S., & Reyes, E. (2012). Assessment of carbon sequestration
868 potential in coastal wetlands. In R. Lal, K. Lorenz, R. Huttl, B. U. Schneider, J. von Braun (Eds.),
869 *Recarbonization of the biosphere: ecosystems and the global carbon cycle* (pp. 517–531). New
870 York: Springer.

871 Morris, J., & Sundberg, K. (2020). Aboveground biomass data from control sites in a *Spartina*
872 *alterniflora*-dominated salt marsh at Law's Point, Rowley River, Plum Island Ecosystem LTER,
873 MA. Environmental Data Initiative.

874 Mudd, S. M., Fagherazzi, S., Morris, J. T., & Furbish, D. J. (2004). Flow, sedimentation, and
875 biomass production on a vegetated salt marsh in South Carolina: Toward a predictive model of
876 marsh morphologic and ecologic evolution. In S. Fagherazzi, M. Marani, & L. K. Blum (Eds.),
877 *The ecogeomorphology of tidal marshes* (pp. 165–188). Washington, DC: American Geophysical
878 Union (AGU).

879 Oleson, K. W., et al. (2013). *Technical description of version 4.5 of the Community Land Model*
880 *(CLM); NCAR Tech*. Note NCAR/TN-503+STR; NCAR: Boulder, CO, 2013. DOI:
881 10.5065/D6RR1W7M

882 Osland, M. J., Enwright, N. M., Day, R. H., Gabler, C. A., Stagg, C. L., & Grace, J. B. (2016).
883 Beyond just sea - level rise: Considering macroclimatic drivers within coastal wetland
884 vulnerability assessments to climate change. *Global Change Biology*, **22**, 1–11.

885 Parkinson, R. W., Craft, C., DeLaune, R. D., Donoghue, J. F., Kearney, M., Meeder, J. F., ... &
886 Turner, R. E. (2017). Marsh vulnerability to sea-level rise. *Nature Climate Change*, **7**, 756–756.

887 Reyes, E., White, M. L., Martin, J. F., Kemp, G. P., Day, J. W., & Aravamuthan, V. (2000).
888 Landscape modeling of coastal habitat change in the Mississippi Delta. *Ecology*, **81**, 2331–2349.

889 Reyes, E., Martin, J. F., Day, J. W., Kemp, G. P., & Mashriqui, H. (2004). River forcing at work:
890 Ecological modeling of prograding and regressive deltas. *Wetlands Ecology and Management*,
891 **12**, 103–114.

892 Rodríguez, J. F., Saco, P. M., Sandi, S., Saintilan, N., & Riccardi, G. (2017). Potential increase
893 in coastal wetland vulnerability to sea-level rise suggested by considering hydrodynamic
894 attenuation effects. *Nature Communications*, **8**, 16094.

895 Roe, P. L. (1986). Characteristic-based schemes for the Euler equations. *Annual Review of Fluid*
896 *Mechanics*, **18**, 337–365.

897 Roner, M., D'Alpaos, A., Ghinassi, M., Marani, M., Silvestri, S., Franceschinis, E., & Realdon,
898 N. (2016). Spatial variation of salt-marsh organic and inorganic deposition and organic carbon
899 accumulation: Inferences from the Venice lagoon, Italy. *Advances in Water Resources*, **93**, 276–
900 287.

901 Saintilan, N., Khan, N. S., Ashe, E., Kelleway, J. J., Rogers, K., Woodroffe, C. D., & Horton, B.
902 P. (2020). Thresholds of mangrove survival under rapid sea level rise. *Science*, *368*, 1118–1121.

903 Sandi, S. G., Rodríguez, J. F., Saintilan, N., Riccardi, G., & Saco, P. M. (2018). Rising tides,
904 rising gates: The complex ecogeomorphic response of coastal wetlands to sea-level rise and
905 human interventions. *Advances in Water Resources*, **114**, 135–148.

906 Sandi, S. G., Rodriguez, J. F., Saco, P. M., Saintilan, N., & Riccardi, G. (2021). Accelerated sea-
907 level rise limits vegetation capacity to sequester soil carbon in coastal wetlands: A study case in
908 southeastern Australia. *Earth's Future*, *9*, e2020EF001901.

909 Schellnhuber, H. J., Frieler, K., & Kabat, P. (2014). The elephant, the blind, and the intersectoral
910 intercomparison of climate impacts. *Proceedings of the National Academy of Sciences*, **111**,
911 3225–3227.

912 Schoutens, K., Heuner, M., Minden, V., Schulte Ostermann, T., Silinski, A., Belliard, J. P., &
913 Temmerman, S. (2019). How effective are tidal marshes as nature-based shoreline protection
914 throughout seasons?. *Limnology and Oceanography*, **64**, 1750**–**1762.

915 Schuerch, M., Vafeidis, A., Slawig, T., & Temmerman, S. (2013). Modeling the influence of
916 changing storm patterns on the ability of a salt marsh to keep pace with sea level rise. *Journal of*
917 *Geophysical Research: Earth Surface*, **118**, 84–96.

918 Schuerch, M., Spencer, T., Temmerman, S., Kirwan, M. L., Wolff, C., Lincke, D., ... & Hinkel, J.
919 (2018). Future response of global coastal wetlands to sea-level rise. *Nature*, **561**, 231–234.

Soulsby, R. L. (1997). *Dynamics of marine sands: A manual for practical applications* (248 pp.). London: Thomas Telford.

Tambroni, N., & Seminara, G. (2012). A one-dimensional eco-geomorphic model of marsh response to sea level rise: Wind effects, dynamics of the marsh border and equilibrium. *Journal of Geophysical Research: Earth Surface*, **117**, F03026.

Tan, Z., Zhuang, Q., & Walter Anthony, K. (2015). Modeling methane emissions from arctic lakes: Model development and site-level study. *Journal of Advances in Modeling Earth Systems*, **7**, 459–483.

Tan, Z., Leung, L. R., Li, H.-Y., & Tesfa, T. (2018). Modeling sediment yield in land surface and earth system models: Model comparison, development, and evaluation. *Journal of Advances in Modeling Earth Systems*, **10**, 2192–2213.

Tan, Z., Leung, L. R., Li, H. Y., & Cohen, S. (2022). Representing global soil erosion and sediment flux in Earth System Models. *Journal of Advances in Modeling Earth Systems*, **14**, e2021MS002756.

Tan, Z. (2023). MACES: September 7, 2023 Release (version 2.0) [Software]. Zenodo. https://doi.org/10.5281/zenodo.8326732

Tan, Z., Leung L. R., Liao C., Carniello L., Rodríguez J. F., Saco P. M., & Sandi, S. G. (2023). A Multi-algorithm Approach for Modeling Coastal Wetland Eco-geomorphology [Dataset]. Zenodo. https://doi.org/10.5281/zenodo.8326927

Temmerman, S., Govers, G., Meire, P., & Wartel, S. (2003a). Modelling long-term tidal marsh growth under changing tidal conditions and suspended sediment concentrations, Scheldt estuary, Belgium. *Marine Geology*, **193**, 151–169.

Temmerman, S., Govers, G., Wartel, S., & Meire, P. (2003b). Spatial and temporal factors controlling short-term sedimentation in a salt and freshwater tidal marsh, Scheldt estuary, Belgium, SW Netherlands. *Earth Surf. Processes Landforms*, **28**, 739–755.

Temmerman, S., Meire, P., Bouma, T. J., Herman, P. M., Ysebaert, T., & De Vriend, H. J. (2013). Ecosystem-based coastal defence in the face of global change. *Nature*, **504**, 79–83.

Teuchies, J., Vandenbruwaene, W., Carpentier, R., Bervoets, L., Temmerman, S., Wang, C., ... & Meire, P. (2013). Estuaries as filters: the role of tidal marshes in trace metal removal. *PLOS ONE*, **8**, e70381.

Törnqvist, T. E., Jankowski, K. L., Li, Y. X., & González, J. L. (2020). Tipping points of Mississippi Delta marshes due to accelerated sea-level rise. *Science Advances*, *6*, eaaz5512.

Törnqvist, T. E., Cahoon, D. R., Morris, J. T., & Day, J. W. (2021). Coastal wetland resilience, accelerated sea-level rise, and the importance of timescale. *AGU Advances*, **2**, e2020AV000334.

954 Vafeidis, A. T., Nicholls, R. J., McFadden, L., Tol, R. S., Hinkel, J., Spencer, T., ... & Klein, R. J.
955 (2008). A new global coastal database for impact and vulnerability analysis to sea-level rise.
956 *Journal of Coastal Research*, **24**, 917–924.

957 Vallino, J. (2018). PIE LTER, Hach, OTT RLS measurements of water column depth at 15
958 minute intervals in the lower Plum Island Sound off the Ipswich Bay Yacht Club pier, Ipswich,
959 MA, year 2017 Environmental Data Initiative.

960 Van de Koppel, J., Van der Wal, D., Bakker, J. P., & Herman, P. M. J. (2005). Self-organization
961 and vegetation collapse in salt marsh ecosystems. *The American Naturalist*, **165**, E1–E12.

962 Wang, F., Lu, X., Sanders, C. J., & Tang, J. (2019). Tidal wetland resilience to sea level rise
963 increases their carbon sequestration capacity in United States. *Nature Communications*, **10**, 5434.

964 Ward, N. D., Megonigal, J. P., Bond-Lamberty, B., Bailey, V. L., Butman, D., Canuel, E. A., ...
965 & Hopkinson, C. S. (2020). Representing the function and sensitivity of coastal interfaces in
966 Earth system models. *Nature Communications*, **11**, 2458.

967 Wilson, C. A., Hughes, Z. J., FitzGerald, D. M., Hopkinson, C. S., Valentine, V., & Kolker, A. S.
968 (2014). Saltmarsh pool and tidal creek morphodynamics: Dynamic equilibrium of northern
969 latitude saltmarshes?. *Geomorphology*, **213**, 99–115.

970 Ye, S., & Pontius, R. G. (2016). PIE LTER Land Cover (2013), Plum Island Sound estuary,
971 Massachusetts - Raster Environmental Data Initiative.

972 Zhang, Y., Rowland, J. C., Xu, C., Wolfram, P. J., Svyatsky, D., Moulton, J. D., ... & Pasqualini,
973 D. (2020). Understanding the eco-geomorphologic feedback of coastal marsh under sea level rise:
974 Vegetation dynamic representations, processes interaction, and parametric sensitivity. *Journal of*
975 *Geophysical Research: Earth Surface*, **125**, e2020JF005729.
976

977 **Figure Captions**

978 **Figure 1.** Model framework for algorithmic comparison of model response of coastal wetland to
979 future environmental stresses. The model comparison platform builds on a 1-D coastal
980 hydrodynamic model which simulates the dynamics of sediment, salinity, nutrients, water
981 inundation, bottom shear stress and other hydrodynamic processes over three coastal landscapes.
982 Processes tested in this paper include Mineral accretion and Organic matter accretion; Landward
983 migration and Wave-action erosion will be tested in the future.

984 **Figure 2.** Sketch of the coastal system and notations. L denotes the 1-D transect domain of
985 coastal landscapes with L_f as the domain of tidal flats and L_w as the domain of coastal wetland.
986 MSL is mean sea level, MHT is mean high tide water level, and WL is water level. The notations
987 of H, h and η represent water level relative to MSL, water depth and bottom elevation relative to
988 MSL. H_0 is the water level at the seaward boundary and η_0 is the bottom elevation at the seaward
989 boundary.

990 **Figure 3.** The elevation of 1-D MACES transects (solid lines) for Venice Lagoon, Plum Island
991 Estuary and Hunter Estuary. Horizontal dash lines represent sea levels and vertical dash lines
992 represent the ocean edge of coastal wetland.

993 **Figure 4.** Dynamics of simulated (black solid line) and observed or benchmark (red solid line
994 with dots) water level, significant wave height and bottom shear stress at the two stations (1BF
995 and 2BF) of Venice Lagoon during two time periods: 12/10/2002–12/11/2002 and 4/2/2003–
996 4/4/2003. Black dashed lines in (a), (b), (g) and (h) represent the estimated water depth at the two
997 stations by assuming the water level spatially uniform across the transect. Blue dashed lines in
998 (c), (d), (i) and (j) represent the measured wind speed. Black dashed lines in (e), (f), (k) and (l)
999 represent the simulated current-induced bottom shear stress.

Figure 5. Comparison of simulated (black solid line) and observed (red dashed line) water depth at the channel station at an elevation of -1.45 masl (a and b) and the *Spartina*-dominated saltmarsh station at an elevation of 1.69 masl (c and d) in Plum Island Estuary during two time periods: 7/19/2017–7/22/2017 and 10/7/2017–10/10/2017. Black dashed lines represent the estimated water depth at the two stations by assuming the water level spatially uniform across the transect.

Figure 6. Comparison of simulated (black solid line) and benchmark (red dashed line) water depth at the channel station at an elevation of -0.22 mAHD (a), the mangrove edge station at an elevation of 0.05 mAHD (b), the mangrove interior station at an elevation of 0.38 mAHD (c) and the saltmarsh edge station at an elevation of 0.65 mAHD (d) of Hunter Estuary during 9/28/2004–9/30/2004. Black dashed lines represent the estimated water depth at these stations by assuming the water level spatially uniform across the transect.

Figure 7. Comparison of observed column-integrated suspended sediment concentration (black) with simulated suspended sediment concentration simulated by seven mineral accretion algorithms at the 1BF station of Venice Lagoon during 12/10/2002–12/11/2002.

Figure 8. Comparison of observed column-integrated suspended sediment concentration (black) with suspended sediment concentration simulated by seven mineral accretion algorithms at the channel station at an elevation of -1.45 masl (a) and the *Spartina*-dominated saltmarsh station at an elevation of 1.69 masl (b) in Plum Island Estuary during the period of 7/19/2017–7/22/2017.

Figure 9. Comparison of benchmark column-integrated suspended sediment concentration (black) with suspended sediment concentration simulated by seven mineral accretion algorithms at the channel station at an elevation of -0.22 mAHD (a), the mangrove edge station at an elevation of 0.05 mAHD (b), the mangrove interior station at an elevation of 0.38 mAHD (c) and

1023 the saltmarsh edge station at an elevation of 0.65 mAHD (d) in Hunter Estuary during
1024 9/28/2004–9/30/2004.
1025 **Figure 10.** Comparison of the simulated mean aboveground biomass in July 2002 by four
1026 MACES algorithms (a), comparison of the simulated long-term OM accretion by four MACES
1027 algorithms (b), comparison of the simulated long-term mineral accretion by seven MACES
1028 algorithms (c), and the mean (solid line) and standard deviation (shared area) of the simulated
1029 long-term total accretion and the contribution of OM accretion to total accretion (d) over the
1030 saltmarsh of Venice Lagoon. Black stars in (b) and (c) represent the observed long-term OM and
1031 mineral accretion, respectively.
1032 **Figure 11.** Comparison of the simulated aboveground biomass in July 2018 at three elevation
1033 zones by four MACES algorithms (a), comparison the simulated long-term OM accretion by four
1034 MACES algorithms (b), comparison of the simulated monthly mean aboveground biomass
1035 during 2017–2018 at the LAC station by four MACES algorithms (c), comparison of the
1036 simulated long-term mineral accretion by seven MACES algorithms (d), and the mean (solid line)
1037 and standard deviation (shared area) of the simulated long-term total accretion and the
1038 contribution of OM accretion to total accretion (d) over the Plum Island wetland. Gray bars in (a),
1039 (c) and (d) represent the mean and standard deviation of the observed summer aboveground
1040 biomass, monthly mean aboveground biomass, and long-term mineral accretion, respectively.
1041 **Figure 12.** Comparison of the simulated mean aboveground biomass in July 2004 by four
1042 MACES algorithms (a), comparison of the simulated long-term OM accretion by four MACES
1043 algorithms (b), comparison of the simulated long-term mineral accretion by seven MACES
1044 algorithms (c), and the mean (solid line) and standard deviation (shared area) of the simulated
1045 long-term total accretion and the contribution of OM accretion to total accretion (d) over the

1046 Hunter Estuary wetland. Black stars in (b) and (c) represent the observed long-term OM and
1047 mineral accretion at the mangrove-dominated station of 0.56 mAHD in elevation, respectively.

Table 1. Summary of the MACES-geomor eco-geomorphology algorithms.

Eco-geomorphology	Category	Algorithm
Mineral accretion	Only sediment deposition	F06 (French, 2006); T03 (Temmerman et al., 2003)
	Both sediment deposition and vegetation trapping	KM12 (Kirwan & Mudd, 2012)
	Both sediment deposition and erosion	F07 (Fagherazzi et al., 2007); VDK05 (van de Koppel et al., 2005)
	Sediment deposition, vegetation trapping and erosion	DA07 (D'Alpaos et al., 2007); M12 (Morris et al., 2012)
OM accretion	No growth seasonality and static shoot:root ratio	M12 (Morris et al., 2012)
	Growth seasonality and static shoot:root ratio	DA07 (D'Alpaos et al., 2007); K16 (Kakeh et al., 2016)
	Growth seasonality, dynamic shoot:root ratio and dynamic carbon turnover	KM12 (Kirwan & Mudd, 2012)
Storm surge erosion	Linear function of wave power	L16 (Leonardi et al., 2016)
Landward migration	Inundation and salinity thresholds	R20 (Reyes et al., 2000); R17 (Rodríguez et al., 2017); S18 (Schuerch et al., 2018)

1056 **Table 2.** Characteristics and observational data of the three coastal wetland sites.

Site Name	Location	Tidal range	Wetland	Evaluation data	Data source
Venice Lagoon	45°33′N/12°27′E	0.84 m	Salt marshes	Water level, significant wave height, suspended sediment, bottom shear stress, long-term mineral accretion, long-term OM accretion	Bellucci et al. (2007); Carniello et al. (2011, 2012); Roner et al. (2016)
Plum Island Estuary	42°49′N/70°49′W	4.45 m	Salt marshes	Water level, suspended sediment, aboveground biomass, long-term mineral accretion, long-term OM accretion	Coleman & Kirwan (2020); Giblin (2018, 2019); Morris & Sundberg (2006, 2020); Vallino (2018); Wang et al. (2019); Wilson et al. (2014)
Hunter Estuary	32°55′S/151°48′E	1.11 m	Mangroves, salt marshes	Water level, suspended sediment, long-term mineral accretion, long-term OM accretion	Howe et al. (2009); Sandi et al. (2018); Rodríguez et al. (2017)

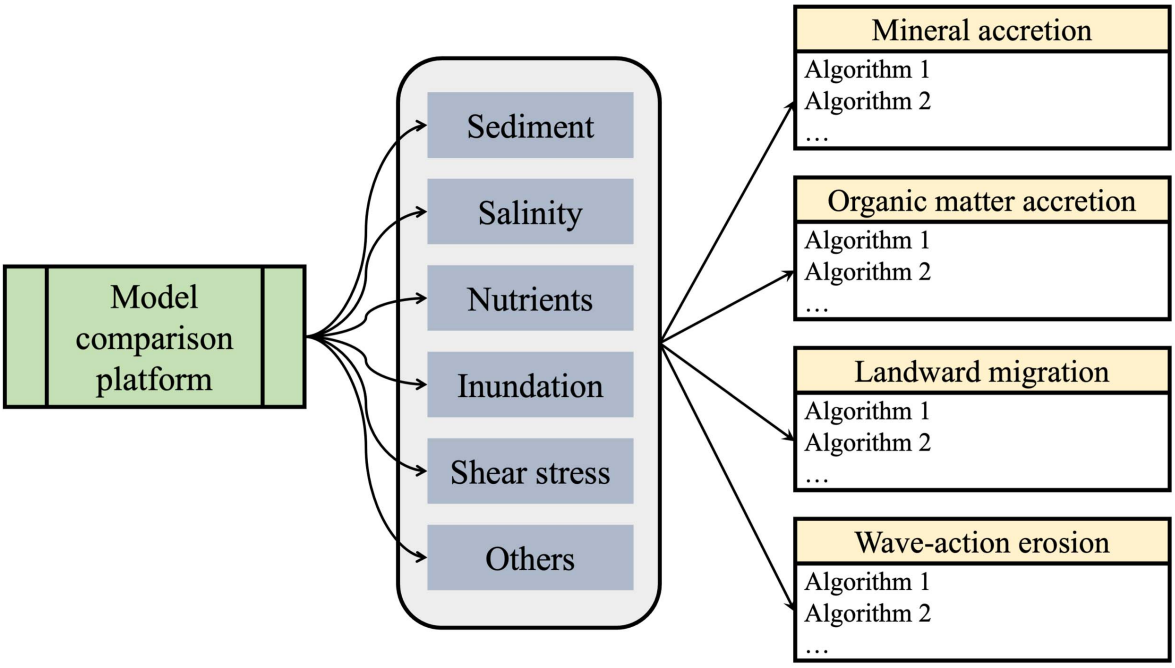
Model comparison platform
Sediment
Salinity
Nutrients
Inundation
Shear stress
Others
Mineral accretion
Algorithm 1
Algorithm 2
…
Organic matter accretion
Algorithm 1
Algorithm 2
…
Landward migration
Algorithm 1
Algorithm 2
…
Wave-action erosion
Algorithm 1
Algorithm 2
…

Figure 1.

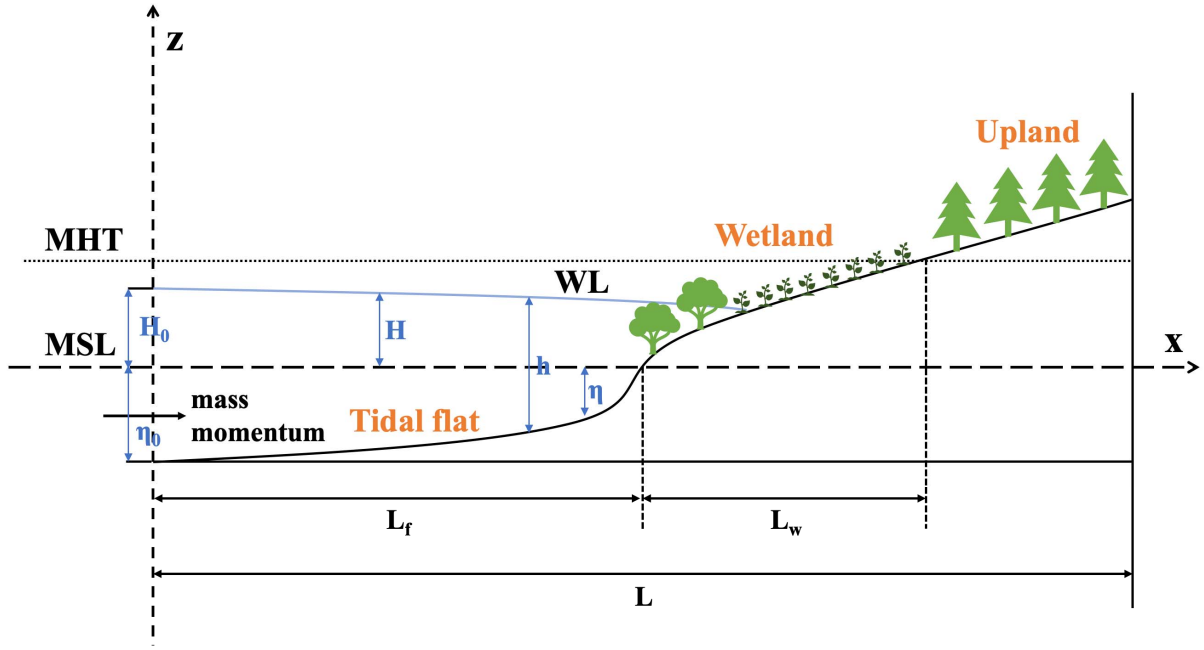
z
Upland
MHT
Wetland
WL
MSL
H0
H
h
η
x
mass
momentum
η0
Tidal flat
Lf
Lw
L

Figure 2.

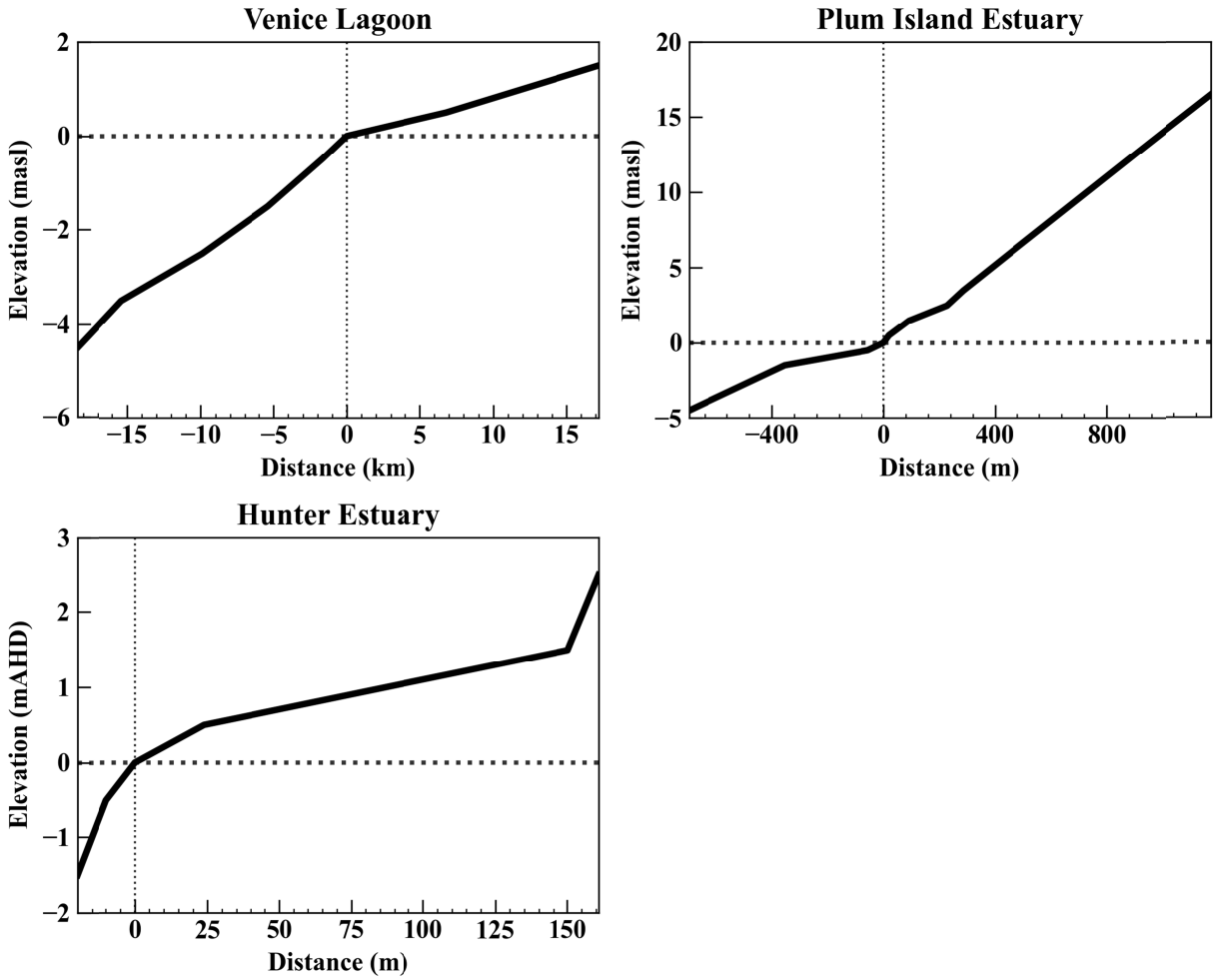
Venice Lagoon
Elevation (masl)
Distance (km)
Plum Island Estuary
Elevation (masl)
Distance (m)
Hunter Estuary
Elevation (mAHD)
Distance (m)

Figure 3.

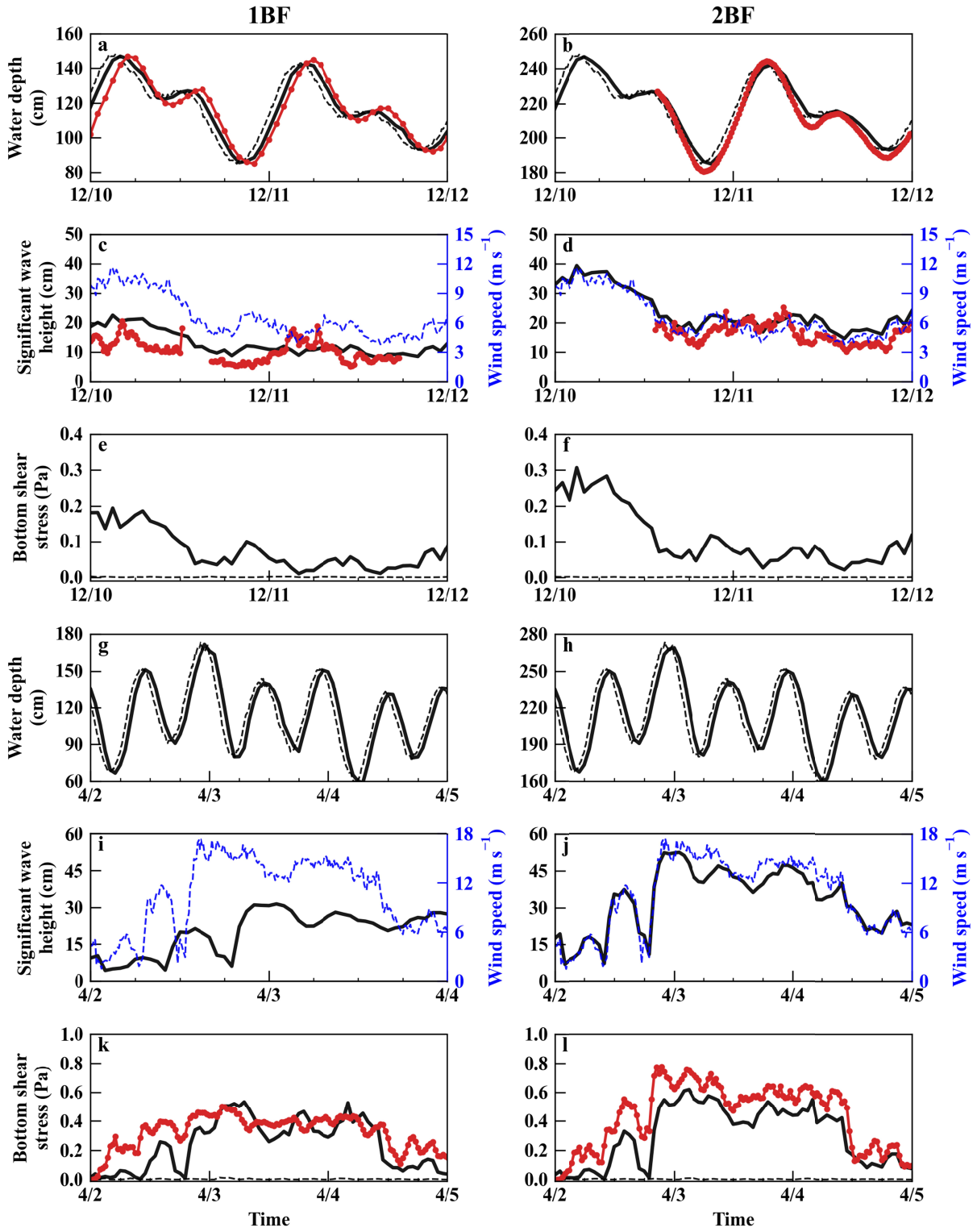

1093

1094 **Figure 4.**

1095

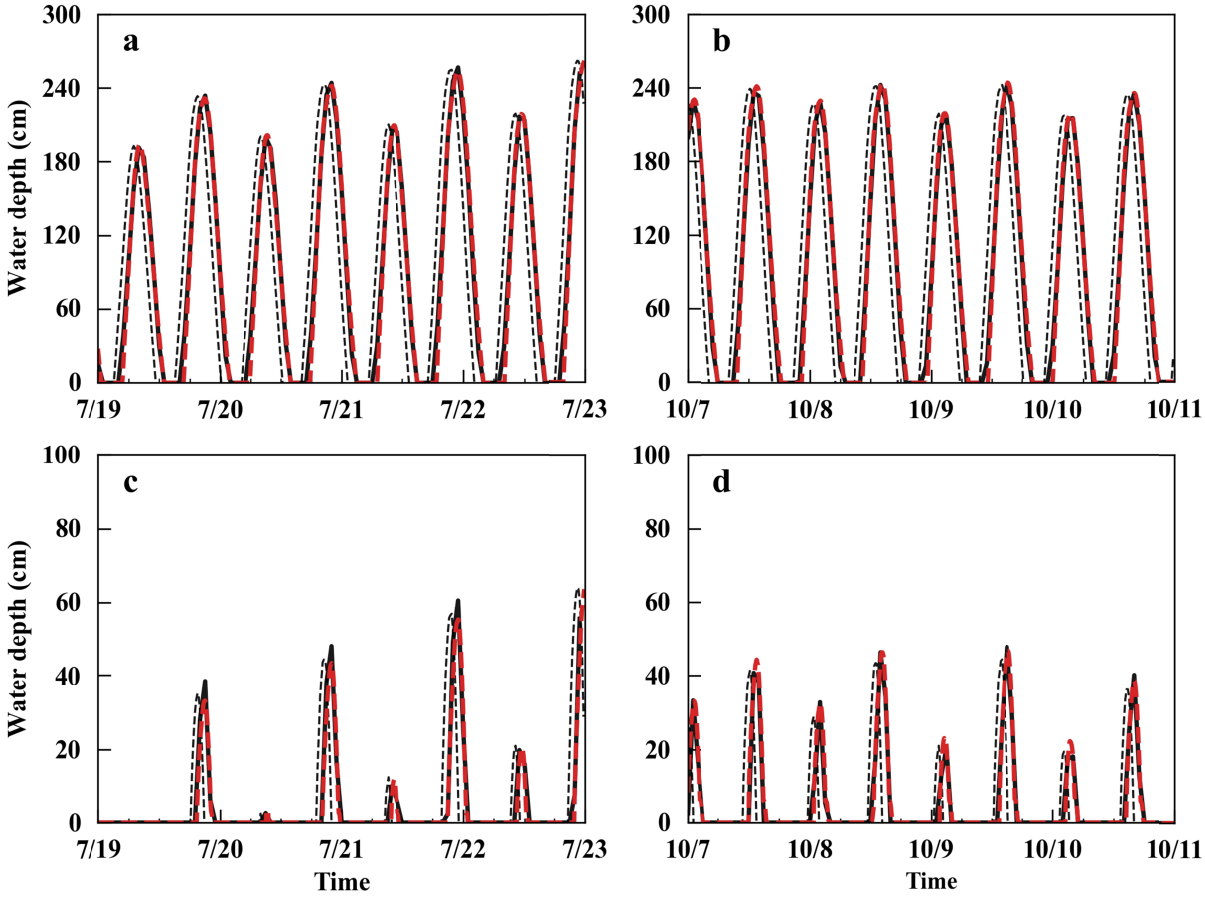
a
b
c
d
Water depth (cm)
Water depth (cm)
Time
Time
300
240
180
120
60
0
100
80
60
40
20
0
7/19
7/20
7/21
7/22
7/23
10/7
10/8
10/9
10/10
10/11

Figure 5.

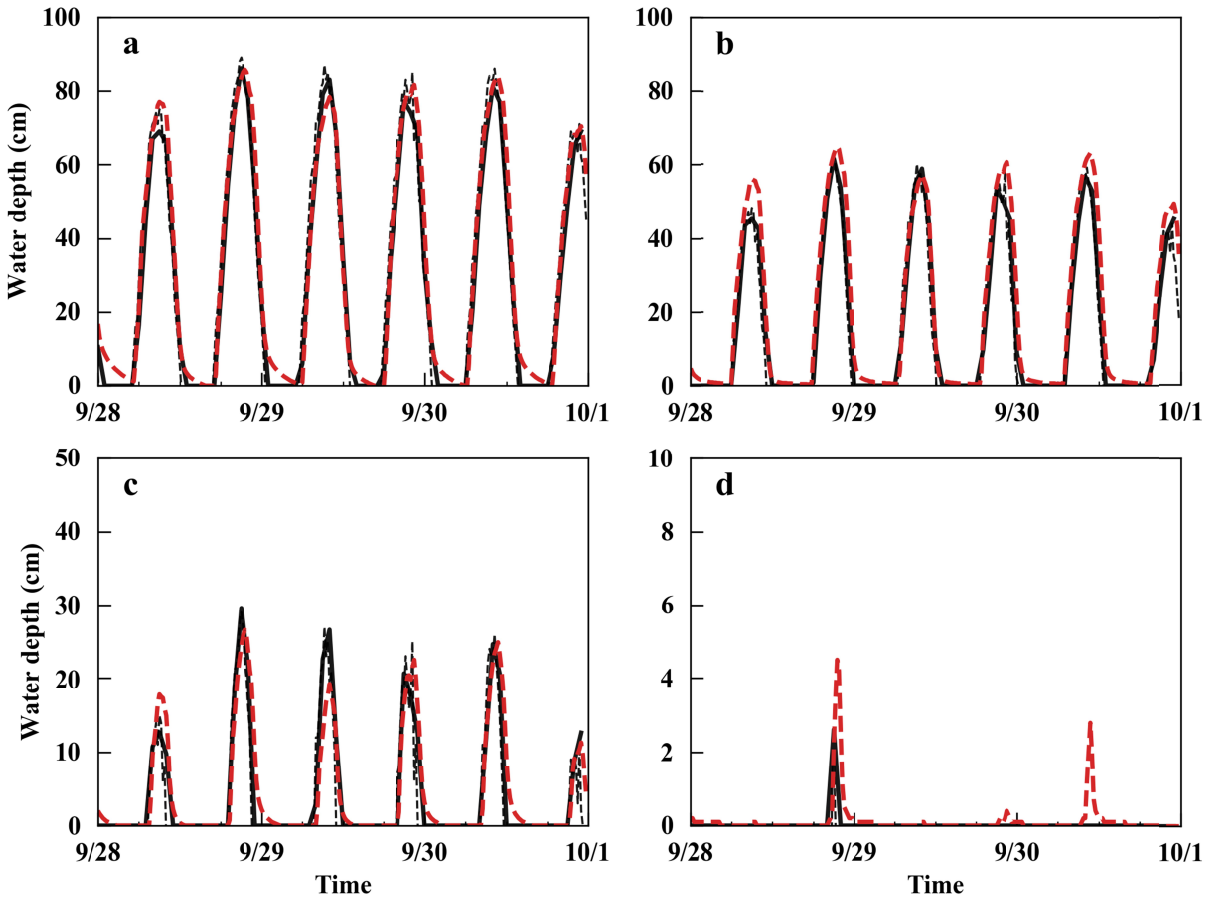

Figure 6.

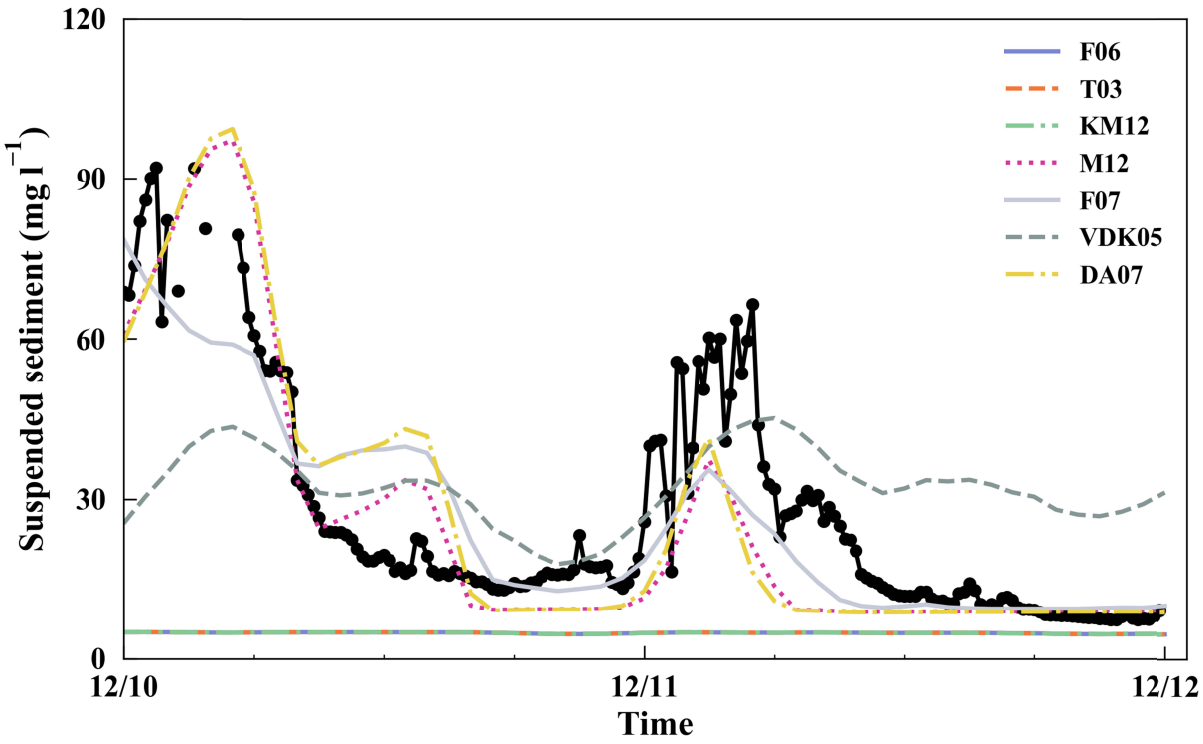
120
90
60
30
0
Suspended sediment (mg l^{-1})
12/10
12/11
12/12
Time
F06
T03
KM12
M12
F07
VDK05
DA07

Figure 7.

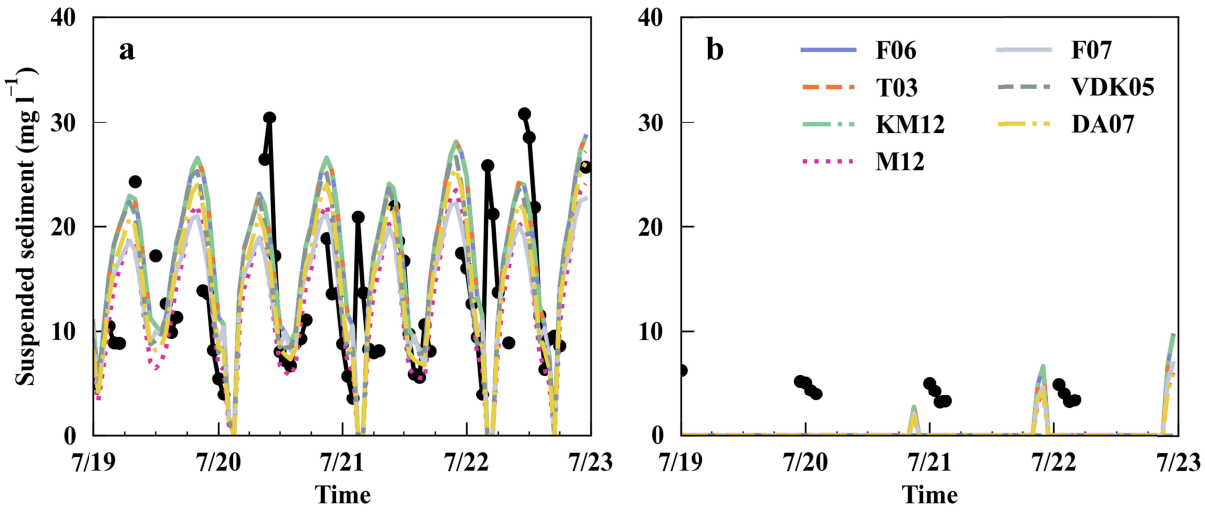
a
b
Suspended sediment (mg l^{-1})
Time
7/19
7/20
7/21
7/22
7/23
0
10
20
30
40
F06
T03
KM12
M12
F07
VDK05
DA07

Figure 8.

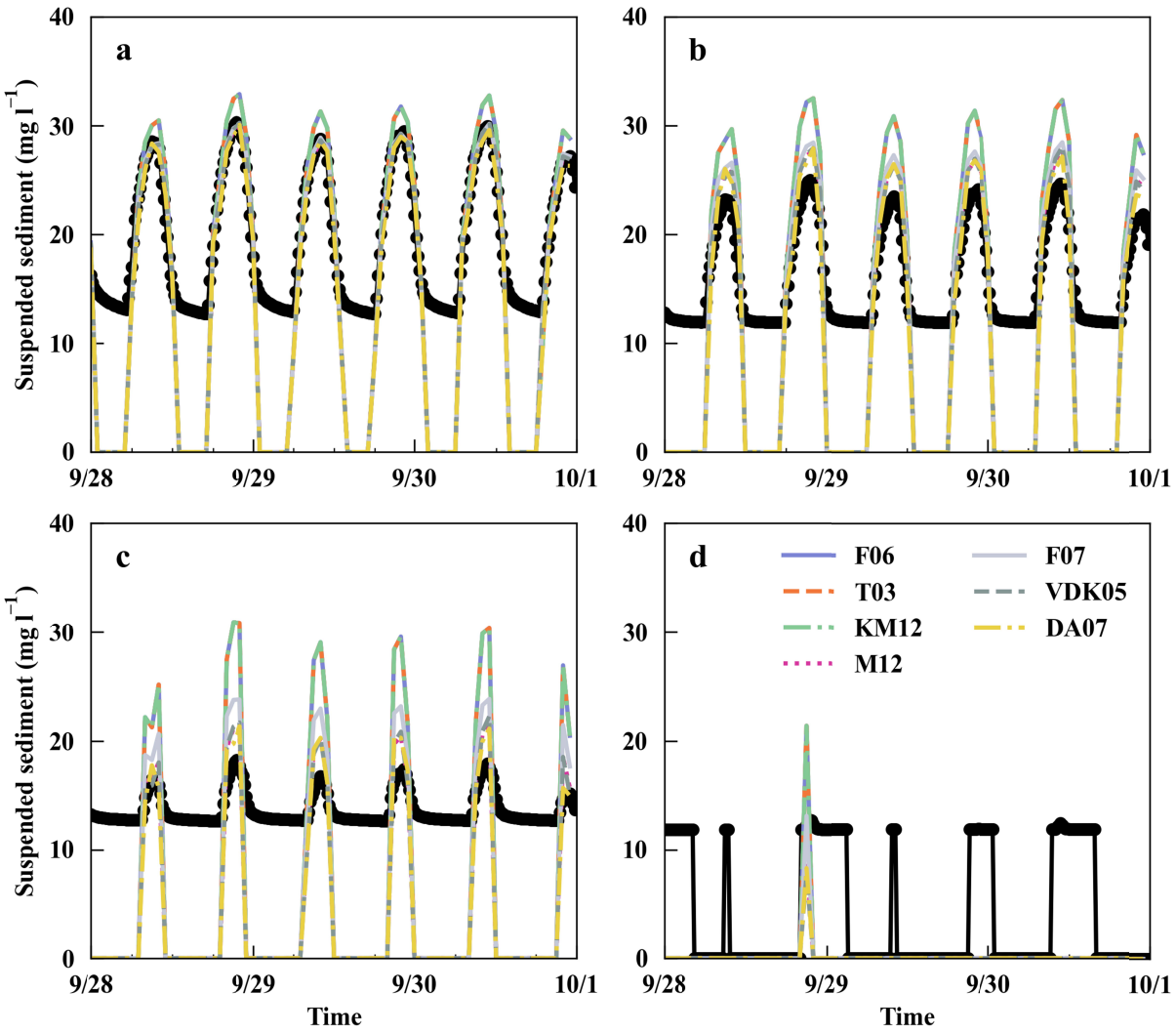
a
b
c
d
Suspended sediment (mg l^{-1})
Time
9/28
9/29
9/30
10/1
0
10
20
30
40
F06
T03
KM12
M12
F07
VDK05
DA07

Figure 9.

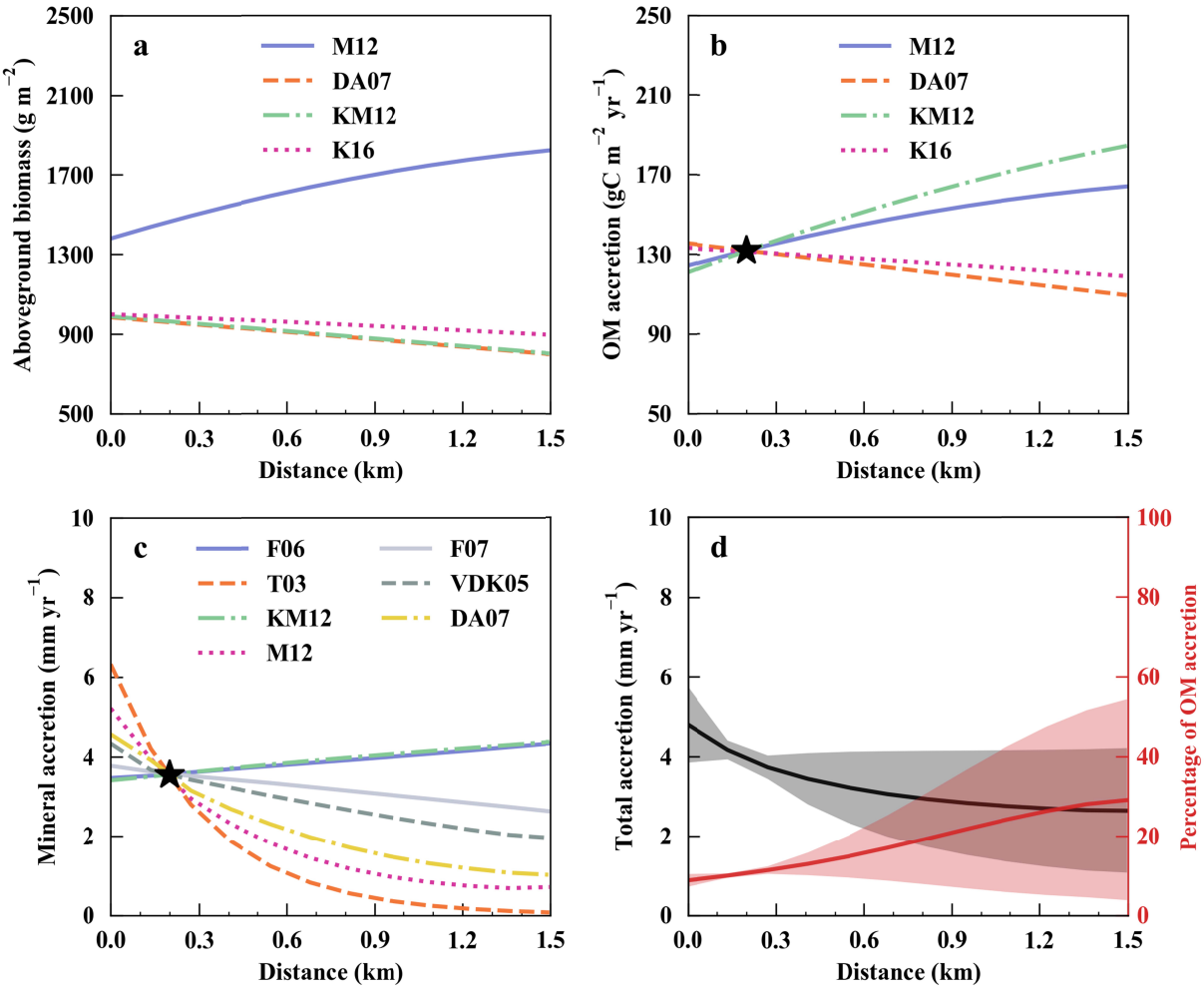
a
M12
DA07
KM12
K16
Aboveground biomass (g m^{-2})
Distance (km)
b
OM accretion (gC m^{-2} yr^{-1})
c
F06
T03
KM12
M12
F07
VDK05
DA07
Mineral accretion (mm yr^{-1})
d
Total accretion (mm yr^{-1})
Percentage of OM accretion

Figure 10.

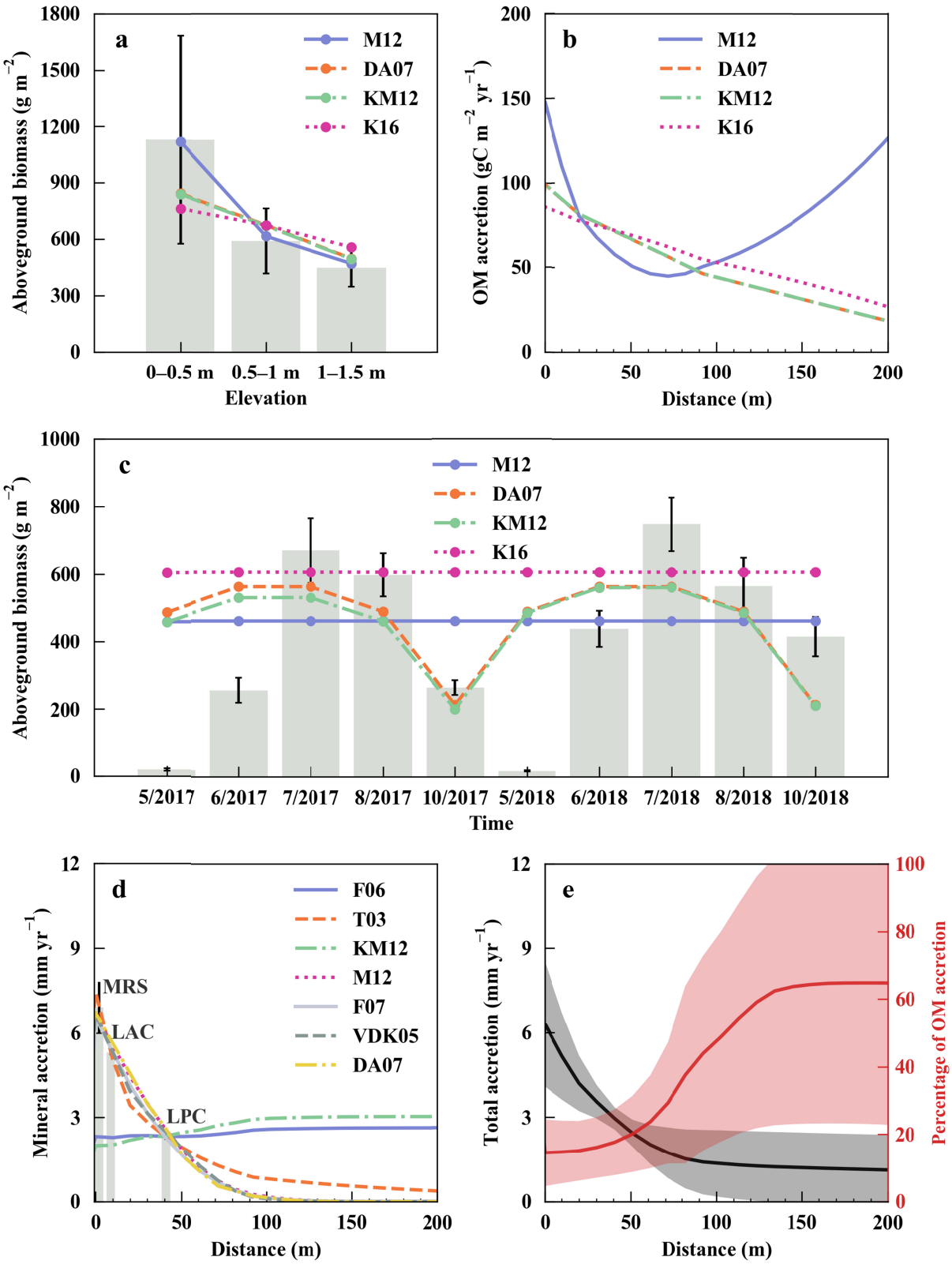

1166

1167 **Figure 11.**

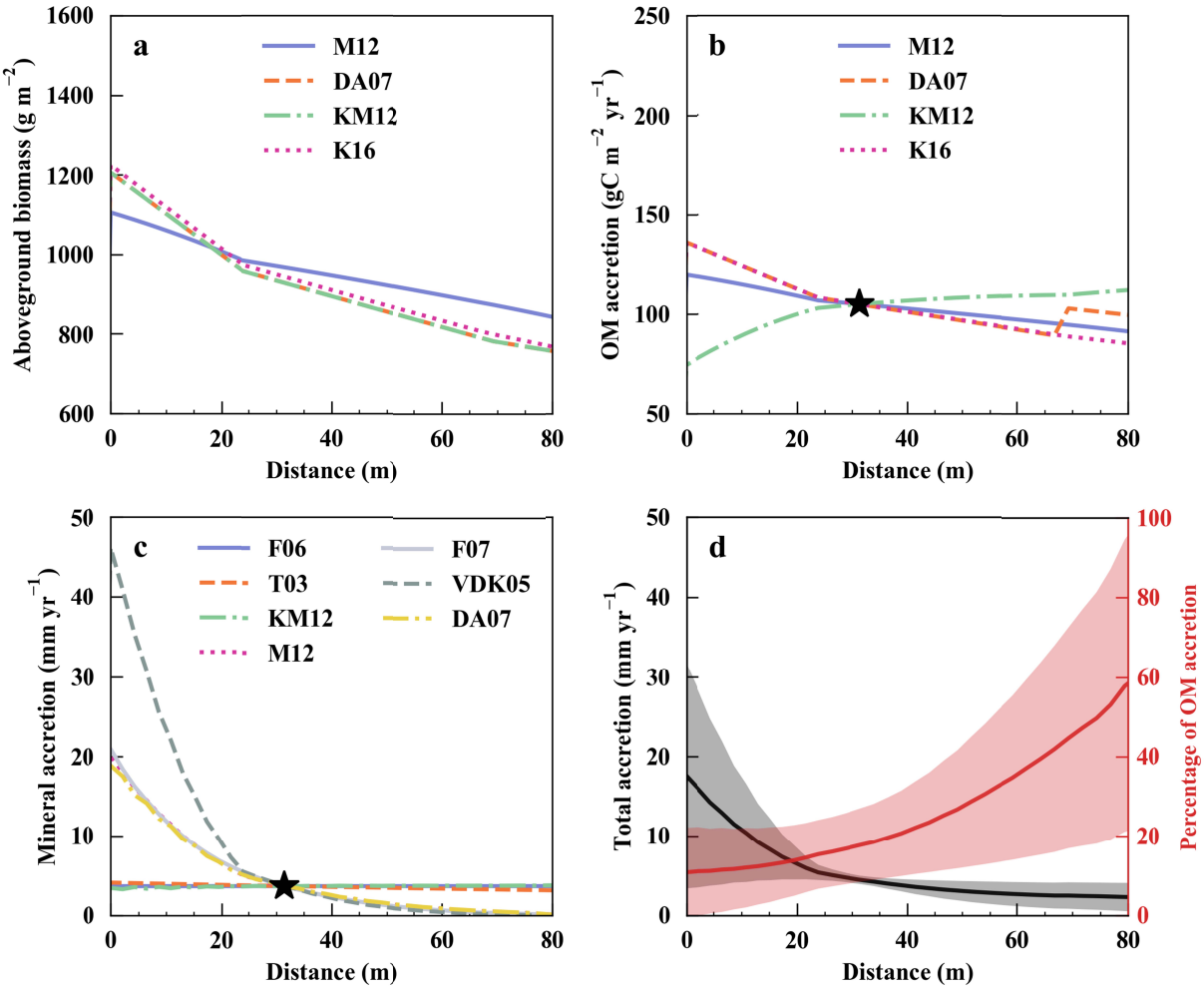

1168

1169 **Figure 12.**

1170

Figure 1.

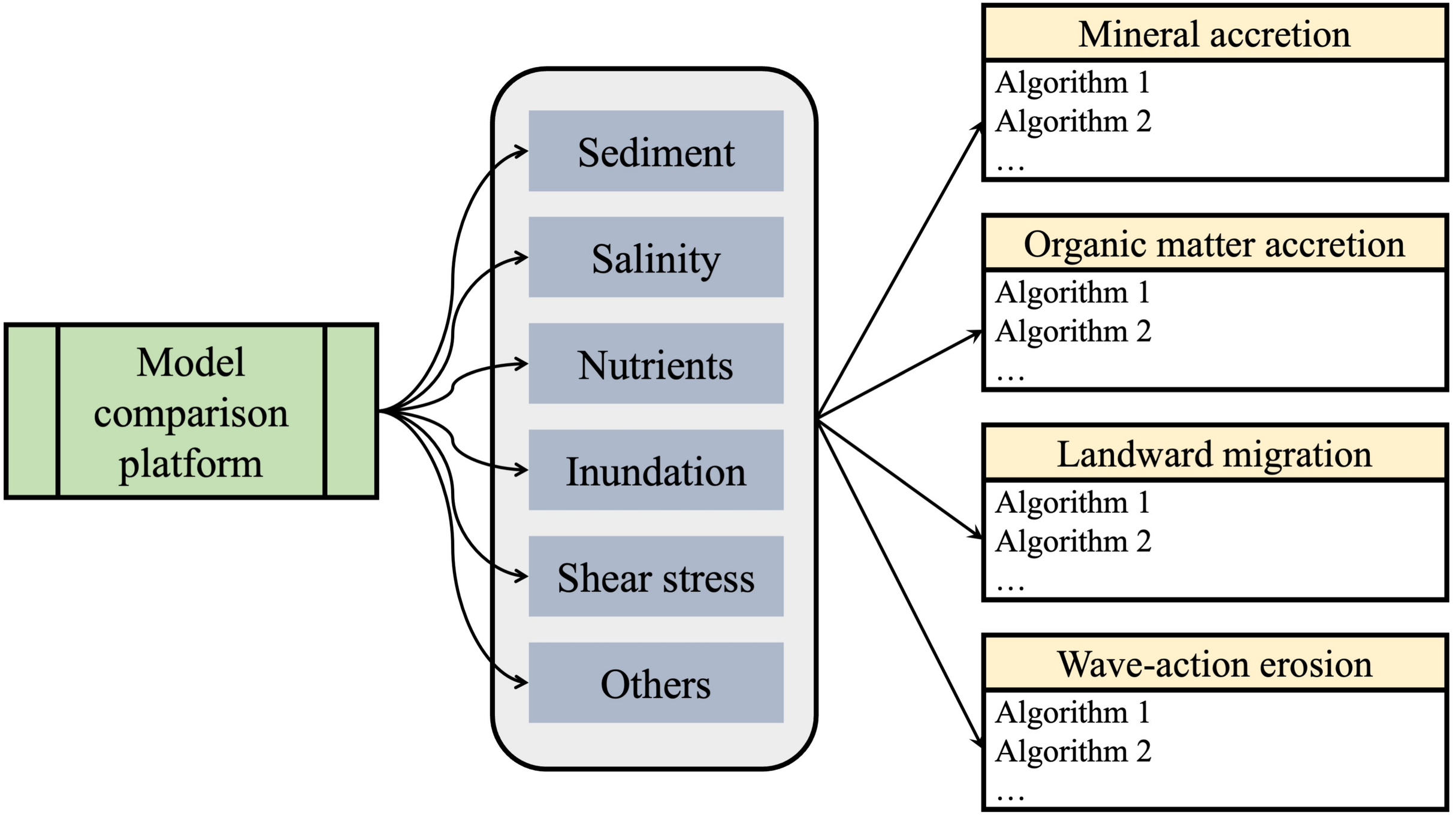
Model comparison platform
Sediment
Salinity
Nutrients
Inundation
Shear stress
Others
Mineral accretion
Algorithm 1
Algorithm 2
…
Organic matter accretion
Algorithm 1
Algorithm 2
…
Landward migration
Algorithm 1
Algorithm 2
…
Wave-action erosion
Algorithm 1
Algorithm 2
…

Figure 2.

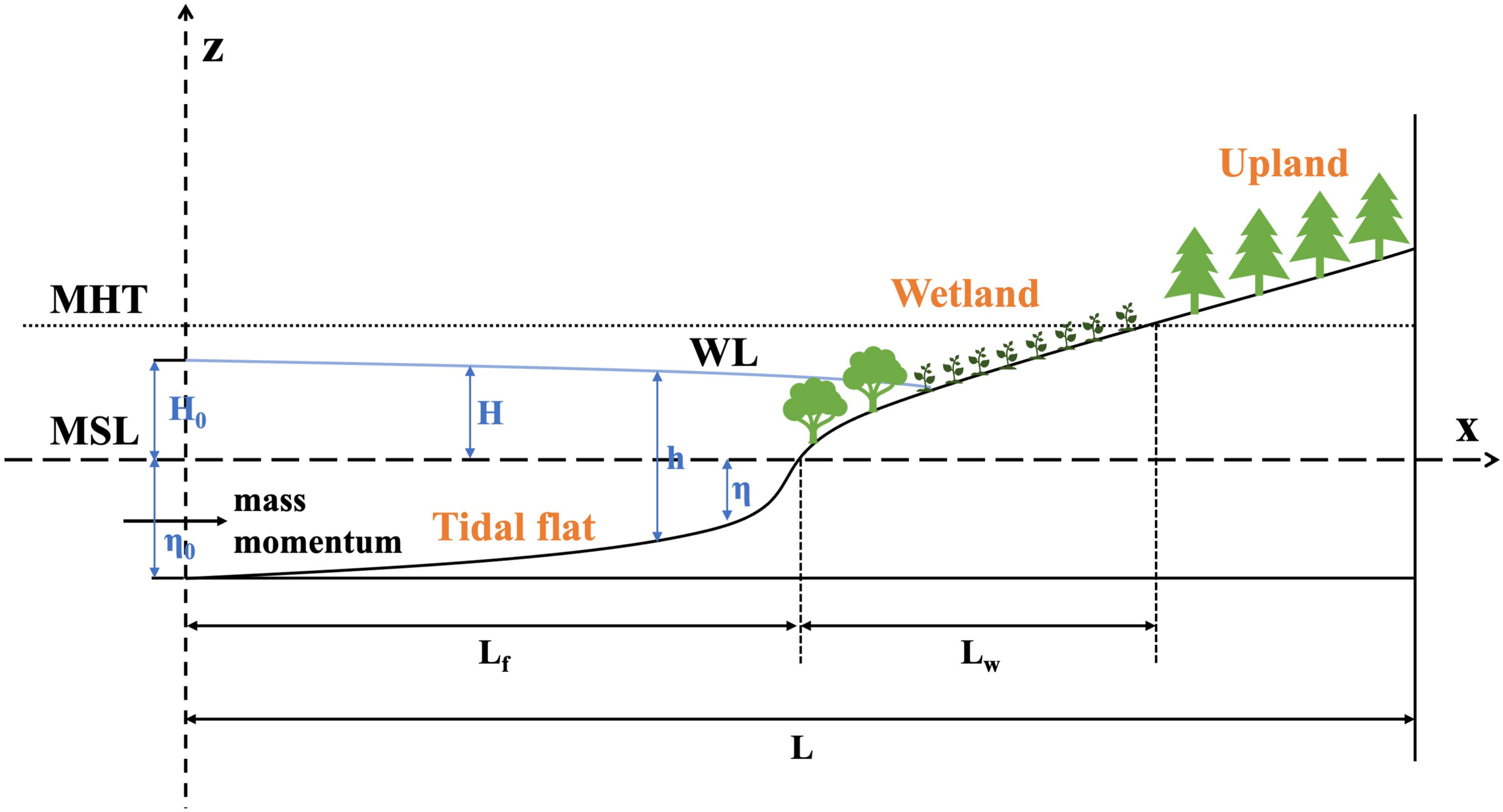
z
MHT
MSL
WL
Wetland
Upland
x
H_0
H
h
η
η_0
mass
momentum
Tidal flat
L_f
L_w
L

Figure 3.

Venice Lagoon

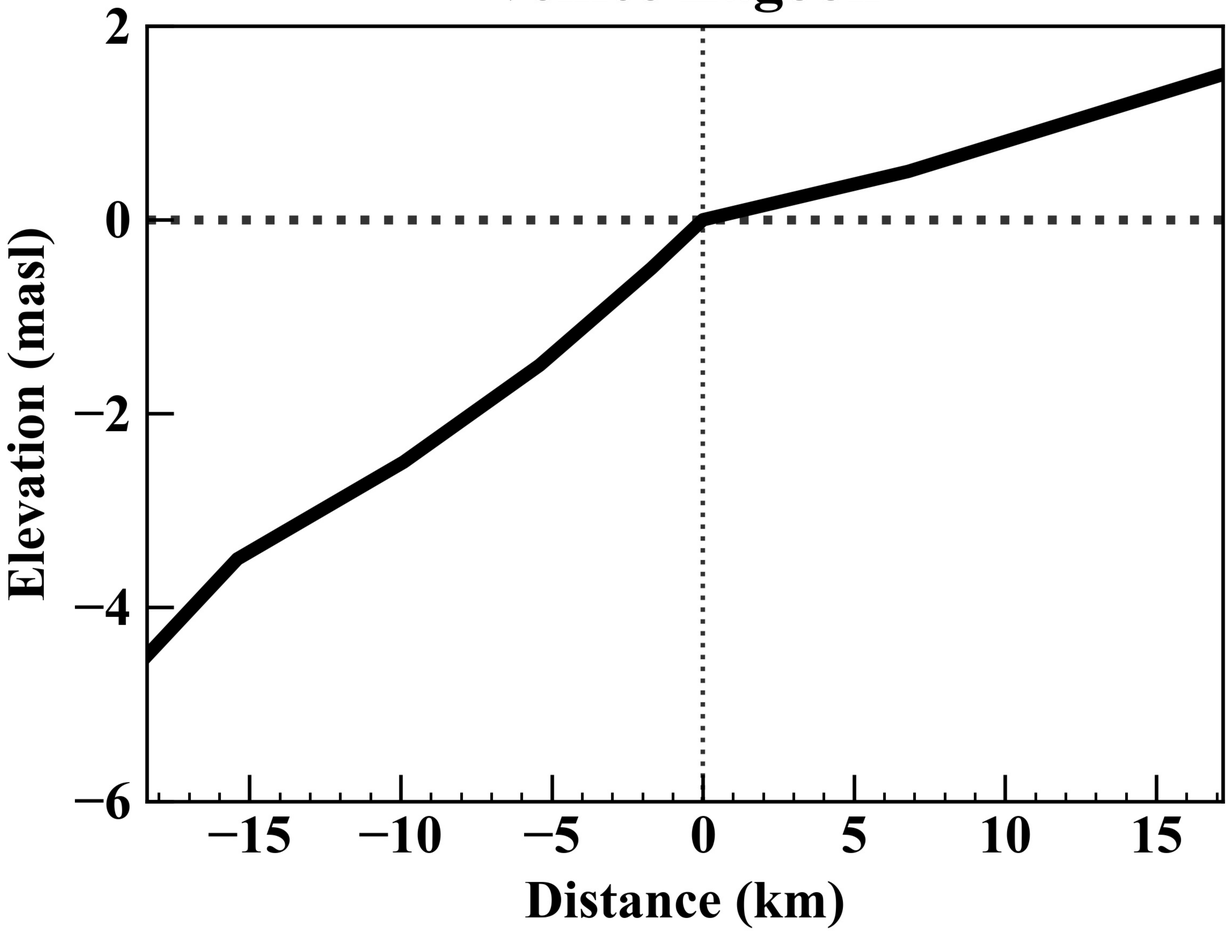

Plum Island Estuary

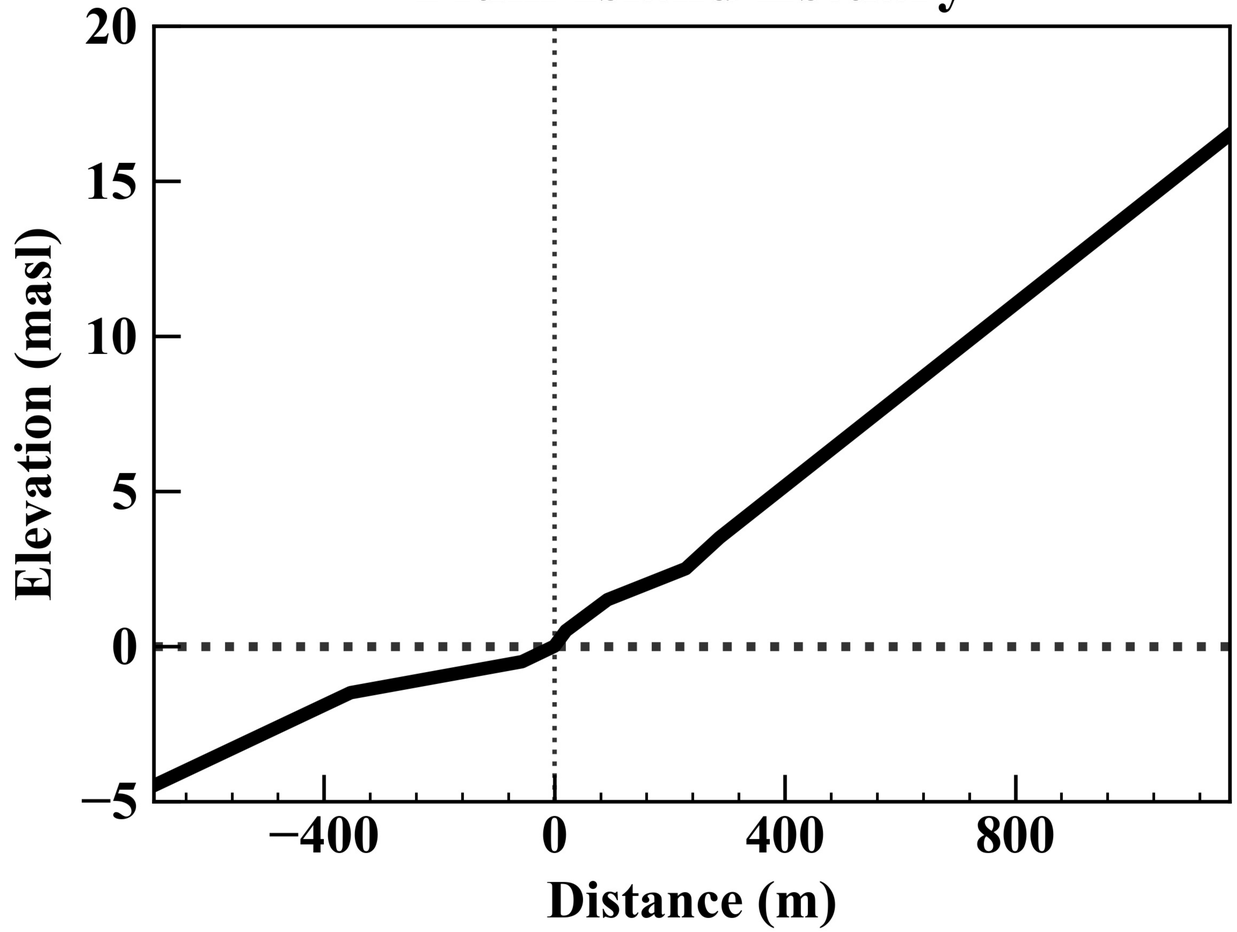

Hunter Estuary

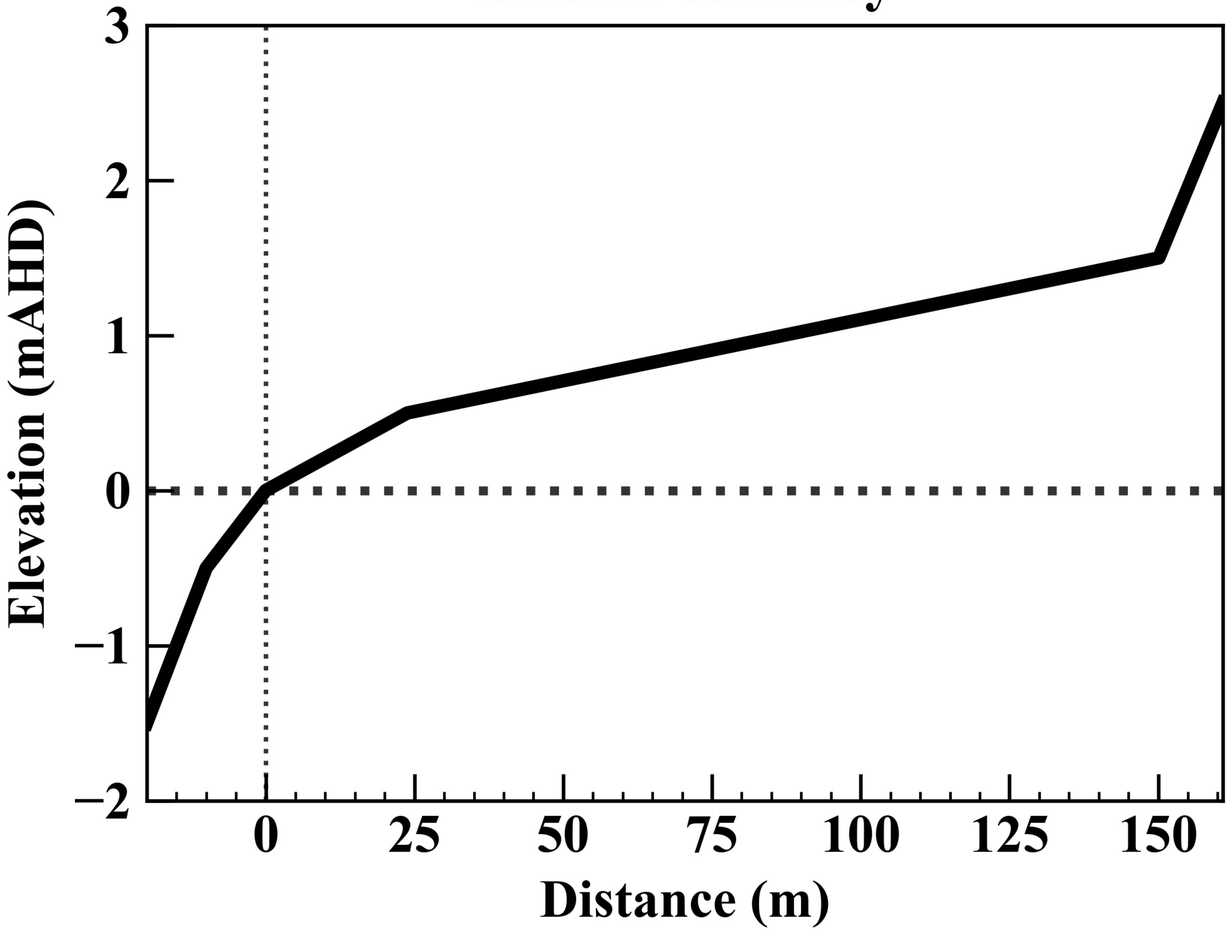

Figure 4.

1BF

2BF

a

b

Water depth (cm)

c

d

Significant wave height (cm)

Wind speed ($m\ s^{-1}$)

e

f

Bottom shear stress (Pa)

g

h

Water depth (cm)

i

j

Significant wave height (cm)

Wind speed ($m\ s^{-1}$)

k

l

Bottom shear stress (Pa)

12/10

12/11

12/12

4/2

4/3

4/4

4/5

Time

Figure 5.

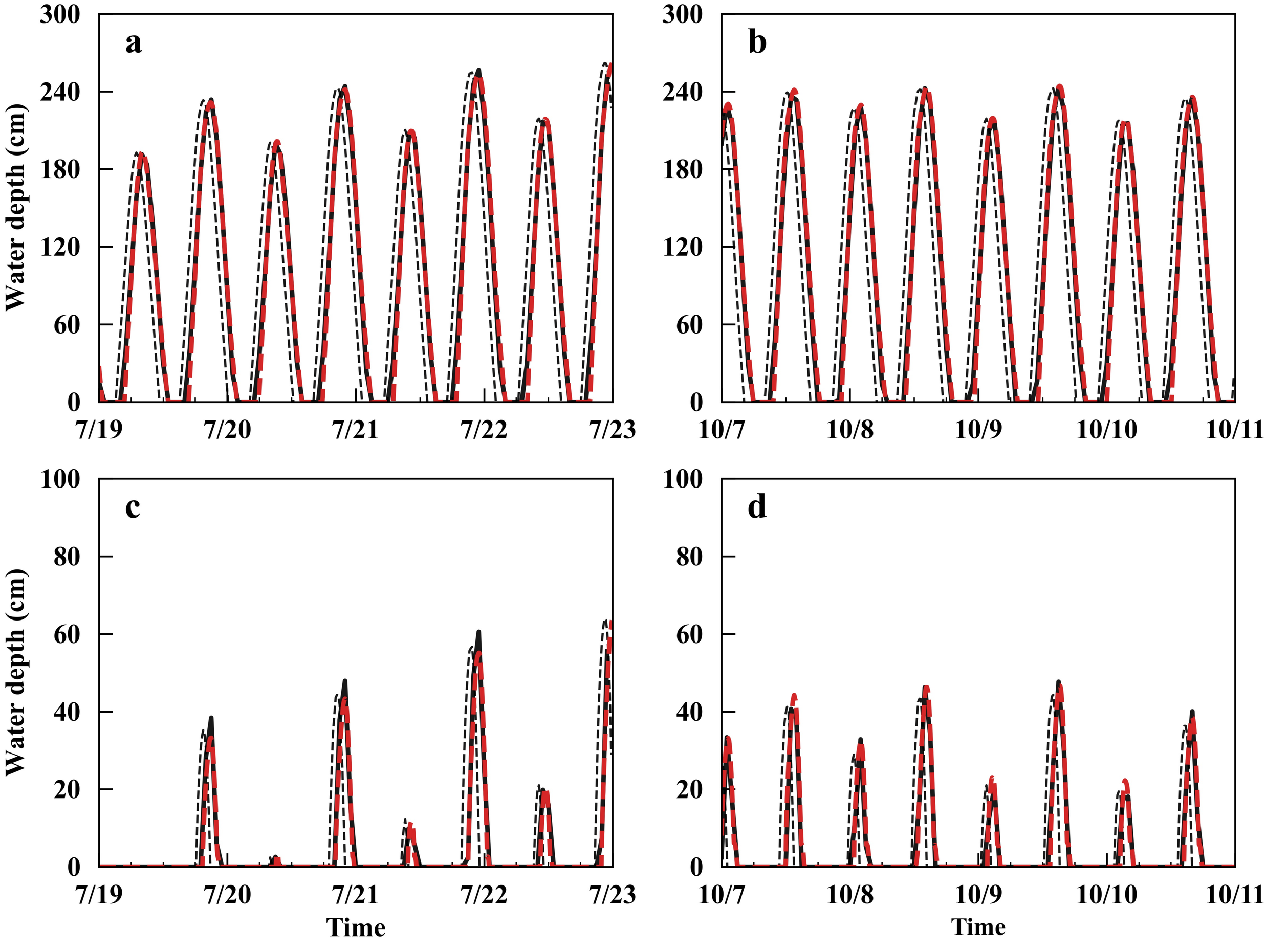
a
b
c
d
Water depth (cm)
Time
300
240
180
120
60
0
100
80
40
20
7/19
7/20
7/21
7/22
7/23
10/7
10/8
10/9
10/10
10/11

Figure 6.

a

b

c

d

Water depth (cm)

Time

9/28

9/29

9/30

10/1

Figure 7.

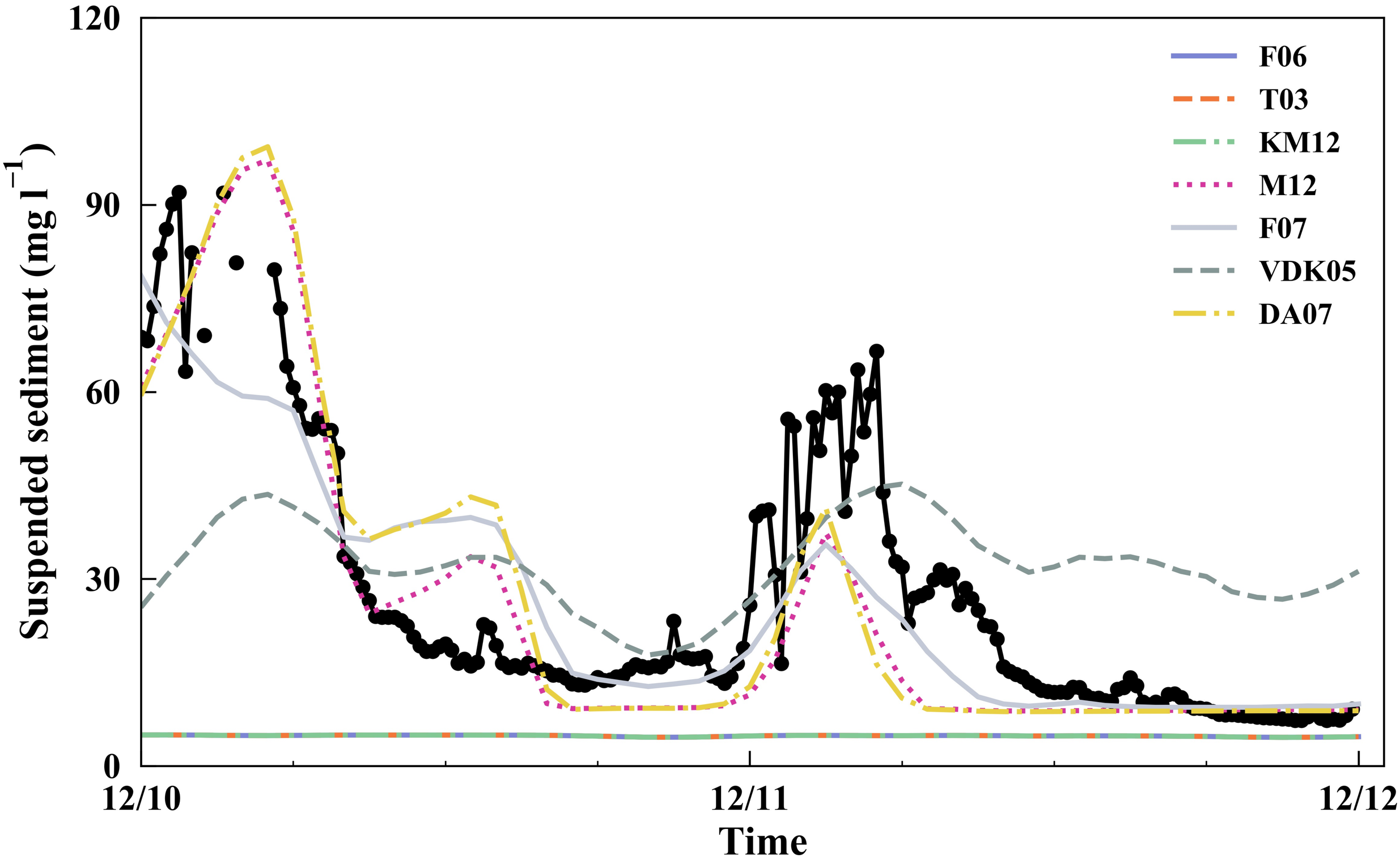
120
90
60
30
0
Suspended sediment (mg l^{-1})
12/10
12/11
12/12
Time
F06
T03
KM12
M12
F07
VDK05
DA07

Figure 8.

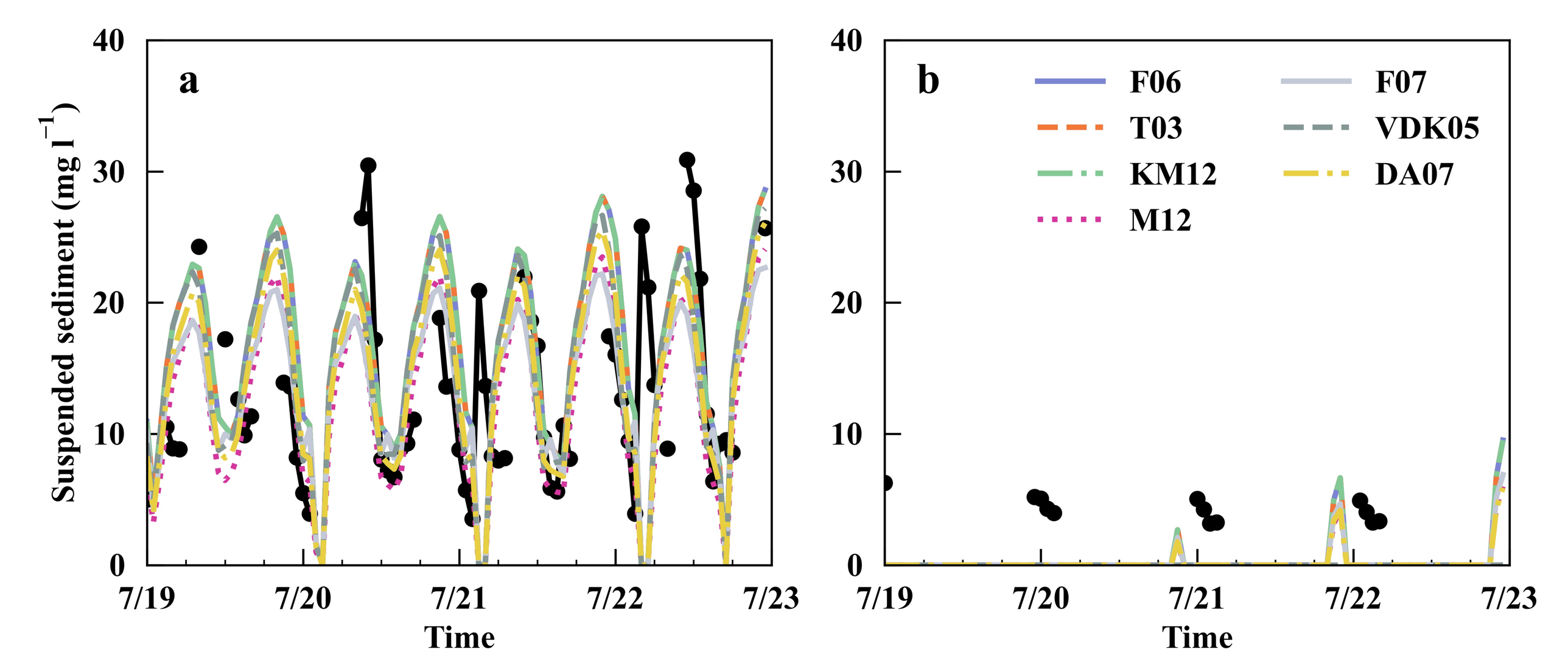
a
b
Suspended sediment (mg l^{-1})
40
30
20
10
0
7/19
7/20
7/21
7/22
7/23
Time
F06
T03
KM12
M12
F07
VDK05
DA07

Figure 9.

a

b

c

d

Suspended sediment (mg l^{-1})

0
10
20
30
40

9/28
9/29
9/30
10/1

Time

F06
T03
KM12
M12
F07
VDK05
DA07

Figure 10.

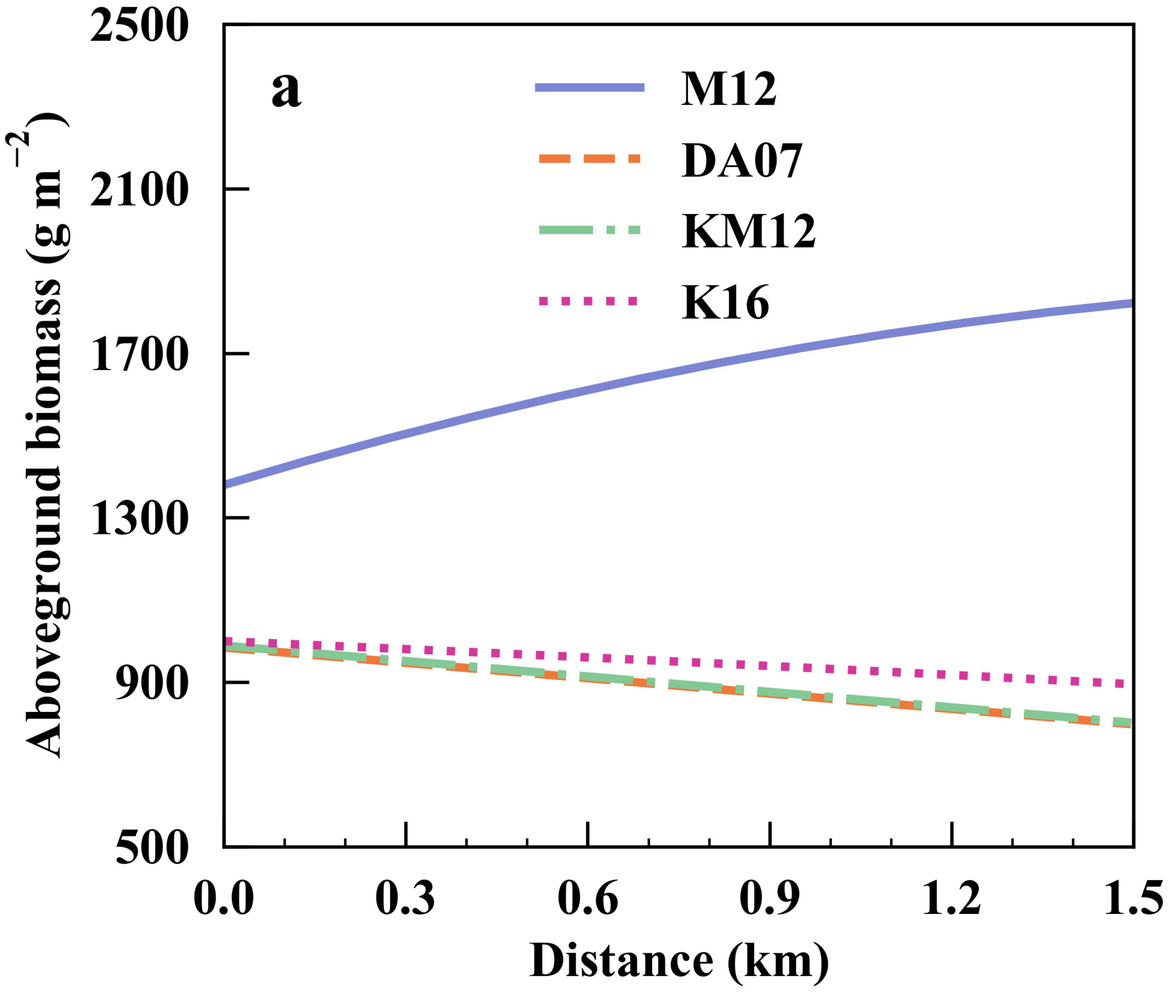
a
M12
DA07
KM12
K16
Aboveground biomass (g m^{-2})
2500
2100
1700
1300
900
500
0.0
0.3
0.6
0.9
1.2
1.5
Distance (km)

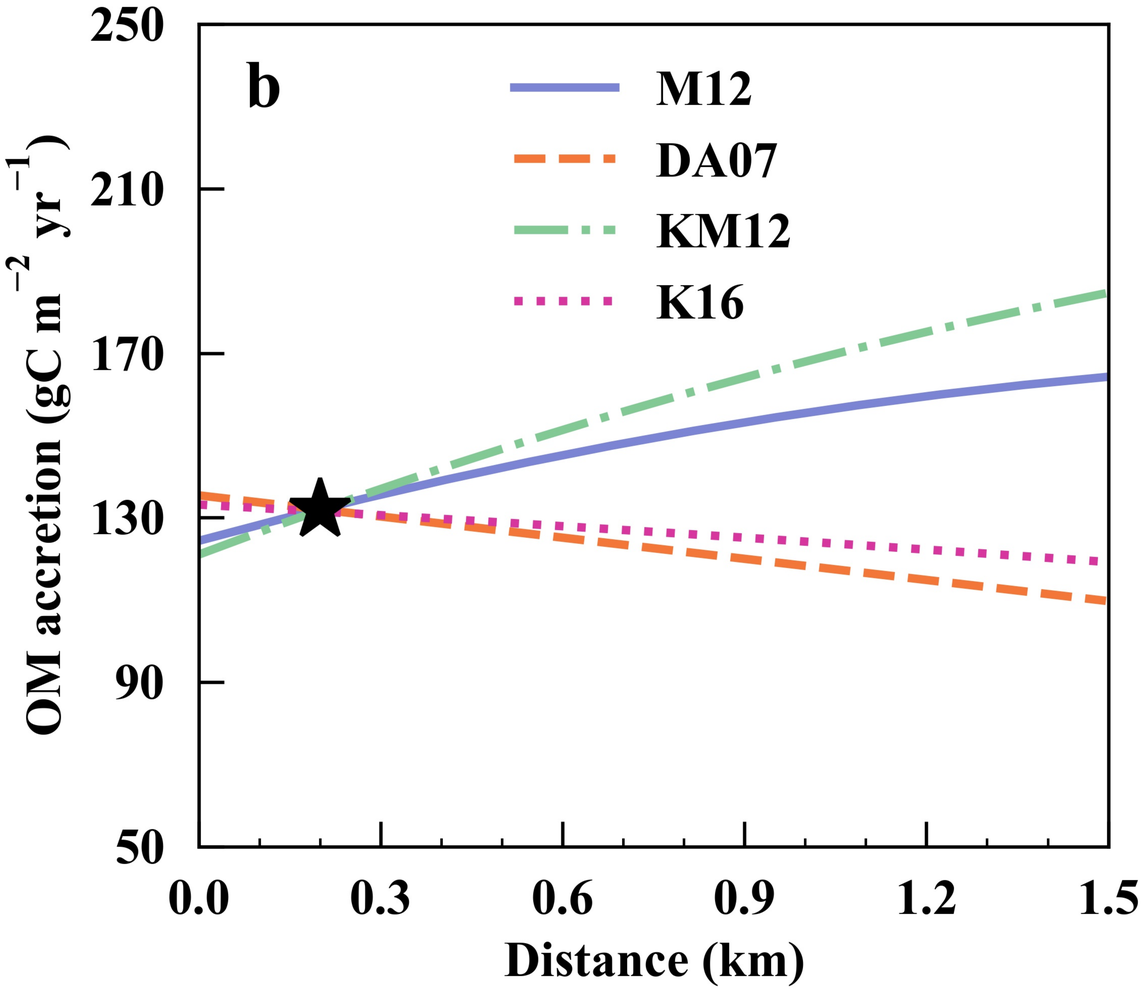
b
M12
DA07
KM12
K16
OM accretion (gC m^{-2} yr^{-1})
250
210
170
130
90
50
0.0
0.3
0.6
0.9
1.2
1.5
Distance (km)

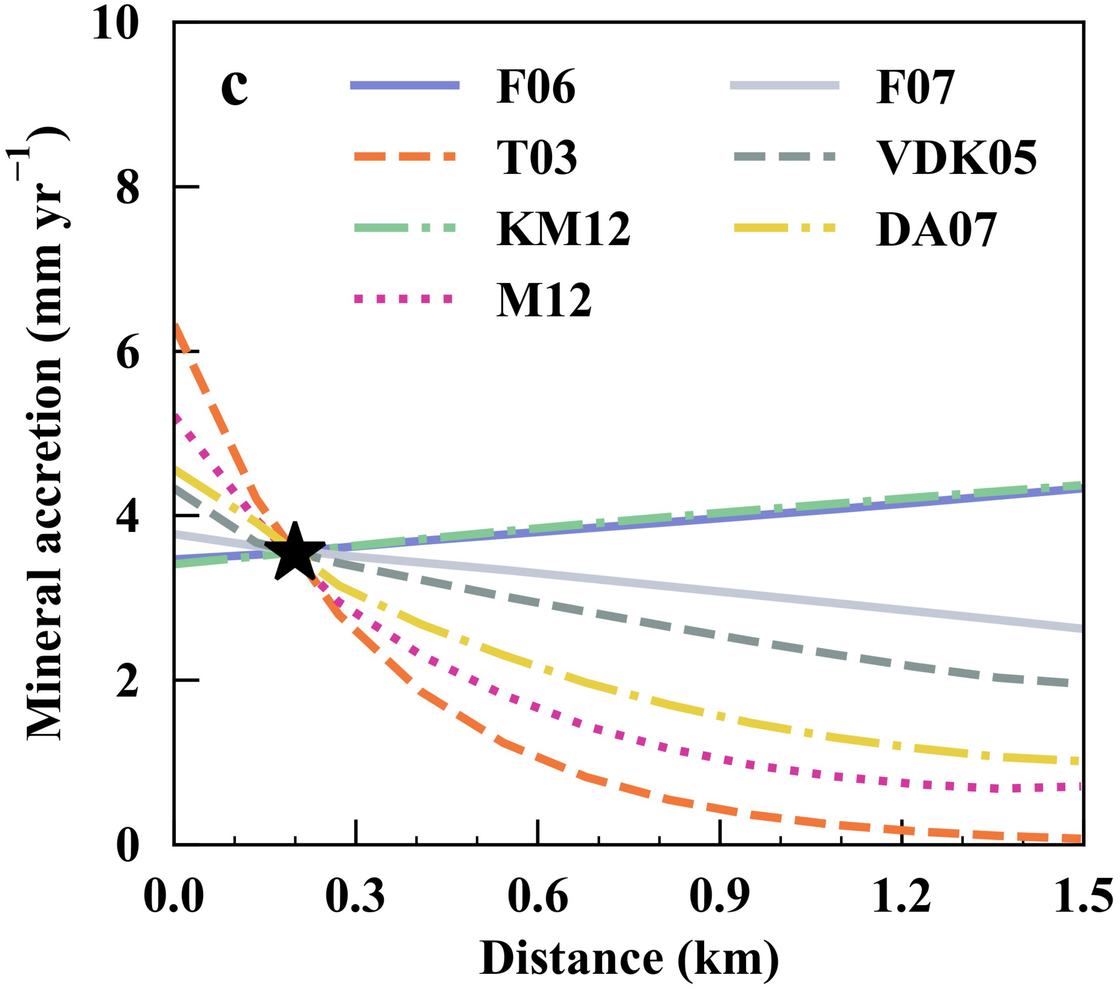
c
F06
T03
KM12
M12
F07
VDK05
DA07
Mineral accretion (mm yr^{-1})
10
8
6
4
2
0
0.0
0.3
0.6
0.9
1.2
1.5
Distance (km)

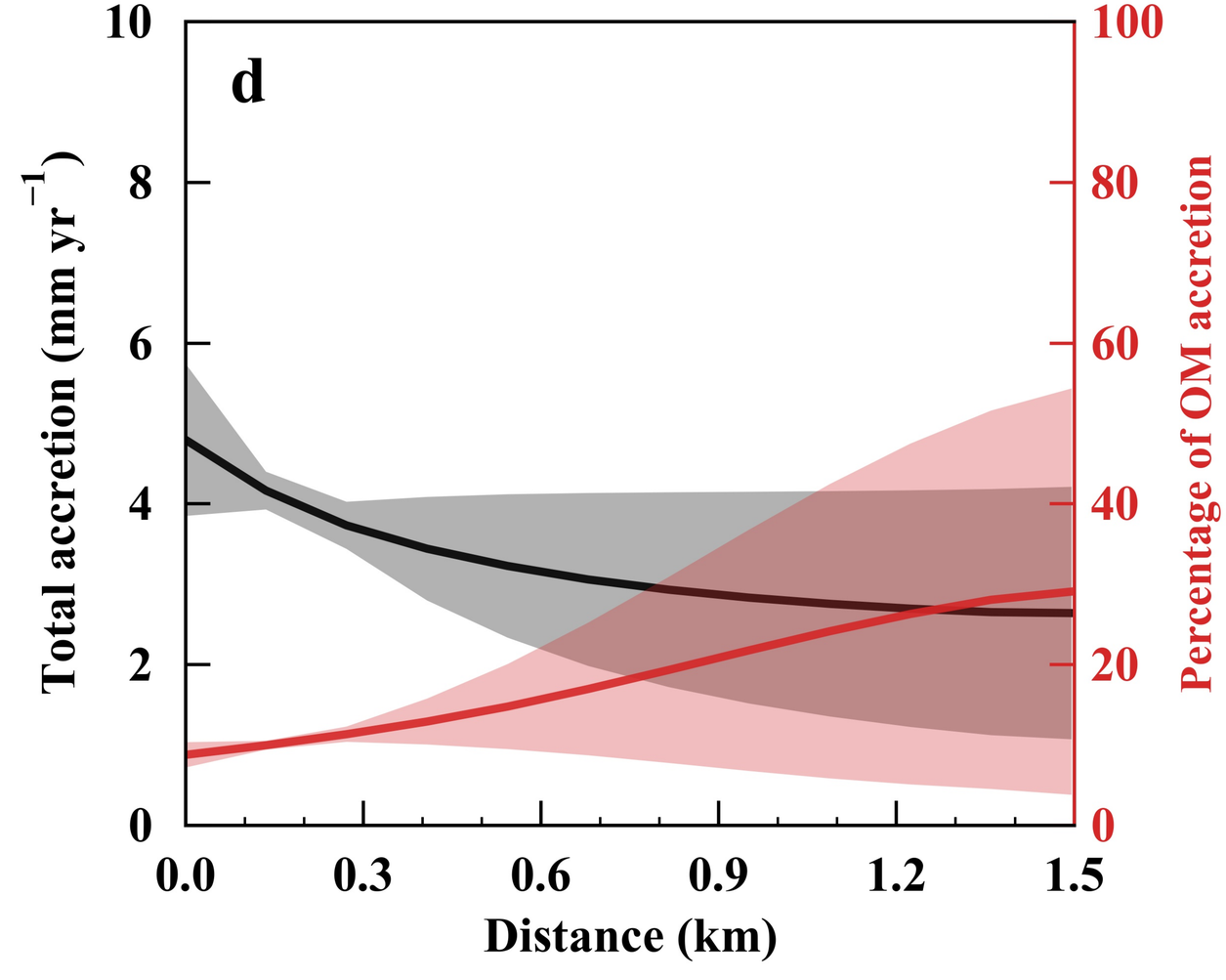
d
Total accretion (mm yr^{-1})
Percentage of OM accretion
10
8
6
4
2
0
100
80
60
40
20
0
0.0
0.3
0.6
0.9
1.2
1.5
Distance (km)

Figure 11.

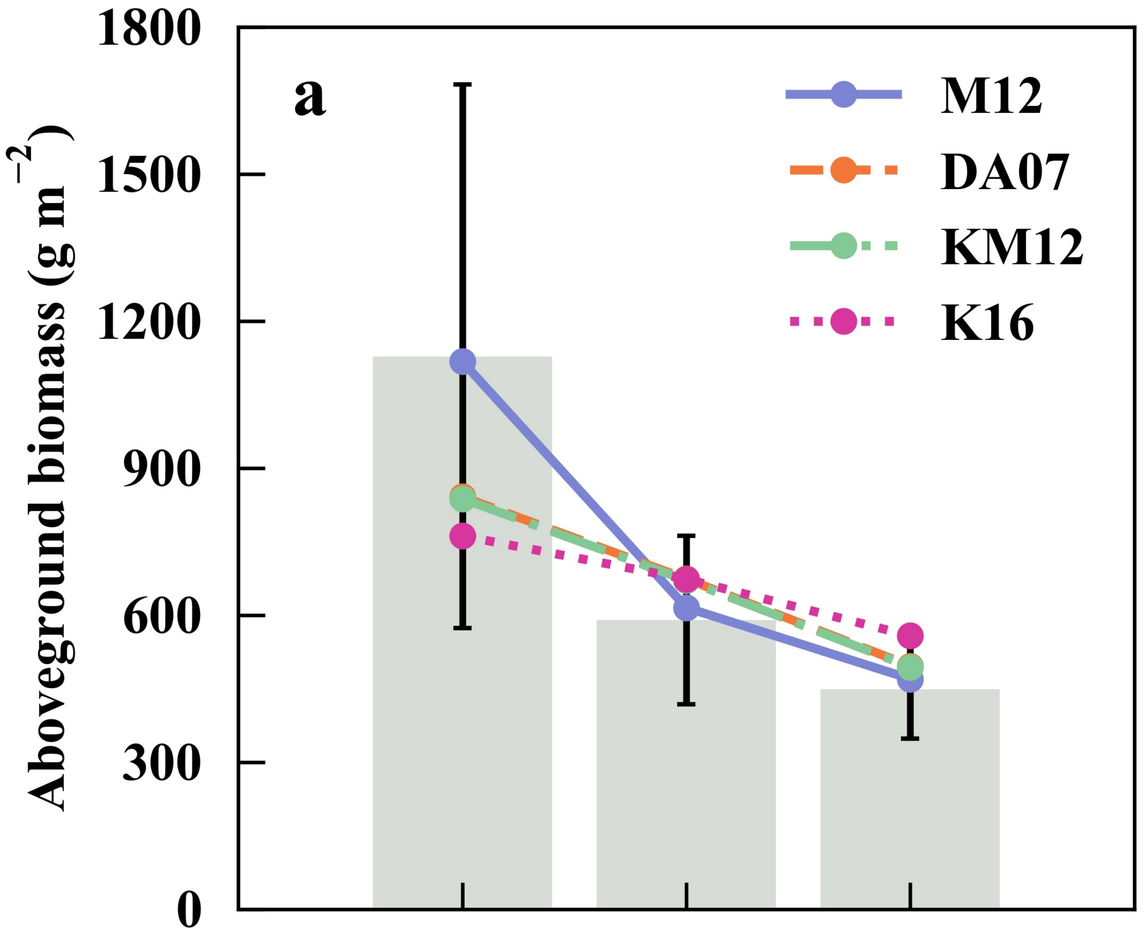
a
M12
DA07
KM12
K16
Aboveground biomass (g m^{-2})
1800
1500
1200
900
600
300
0
0–0.5 m
0.5–1 m
1–1.5 m
Elevation

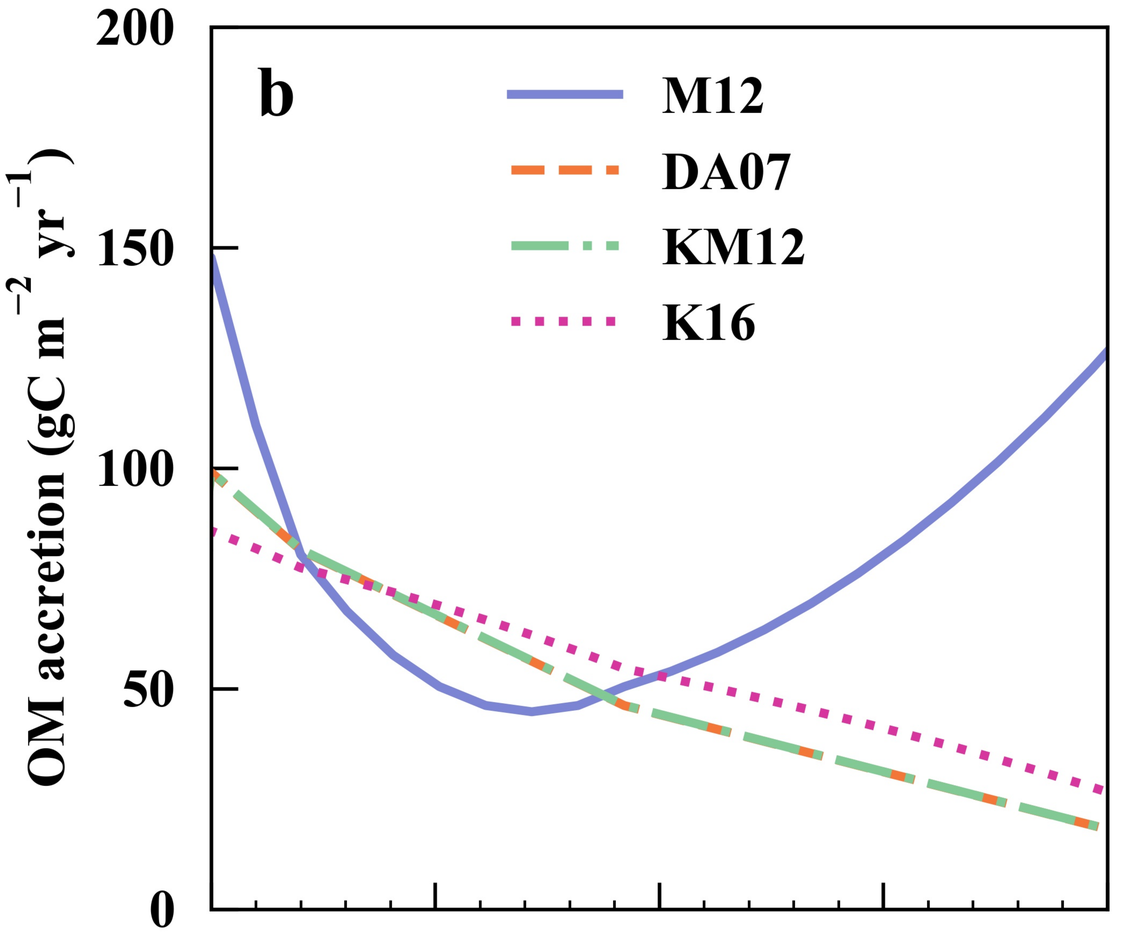
b
M12
DA07
KM12
K16
OM accretion (gC m^{-2} yr^{-1})
200
150
100
50
0
0
50
100
150
200
Distance (m)

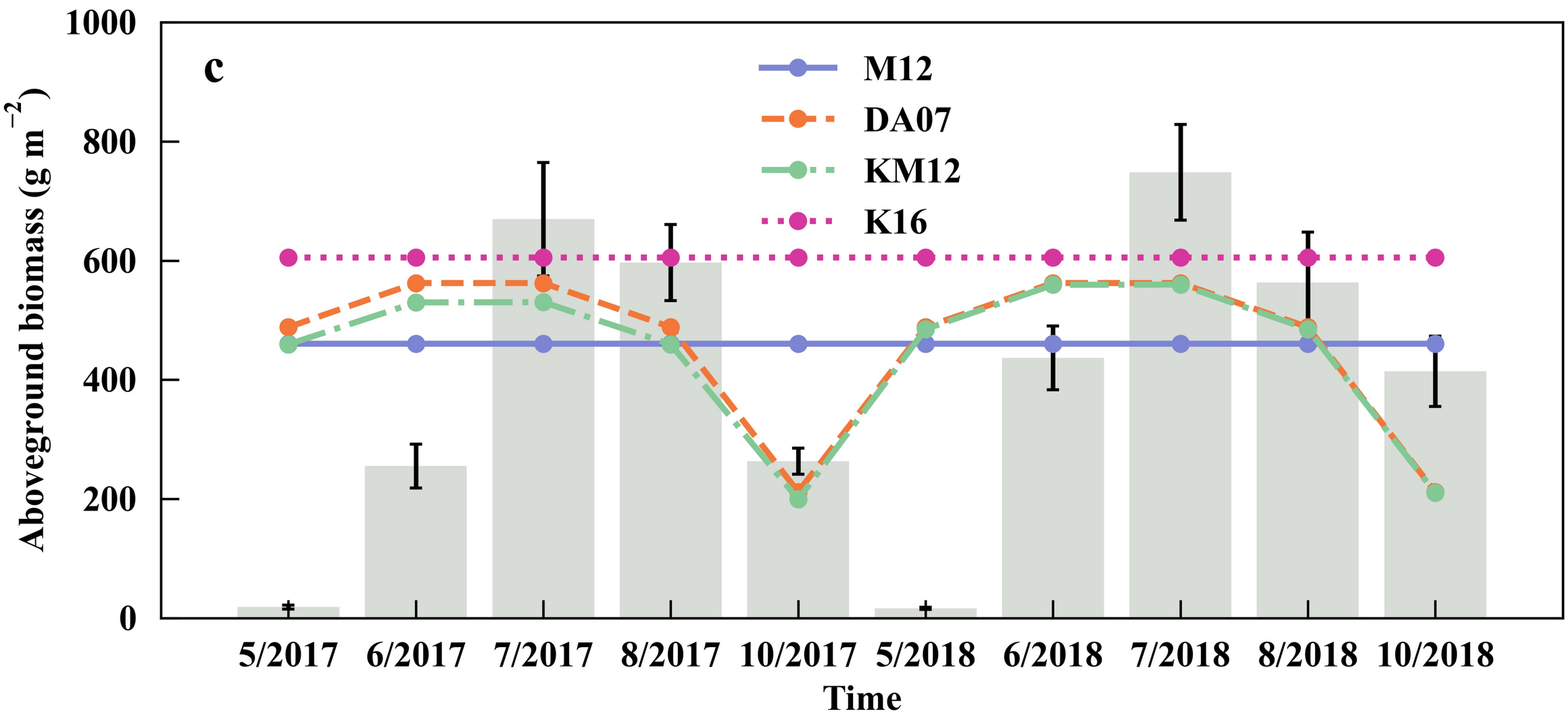
c
M12
DA07
KM12
K16
Aboveground biomass (g m^{-2})
1000
800
600
400
200
0
5/2017
6/2017
7/2017
8/2017
10/2017
5/2018
6/2018
7/2018
8/2018
10/2018
Time

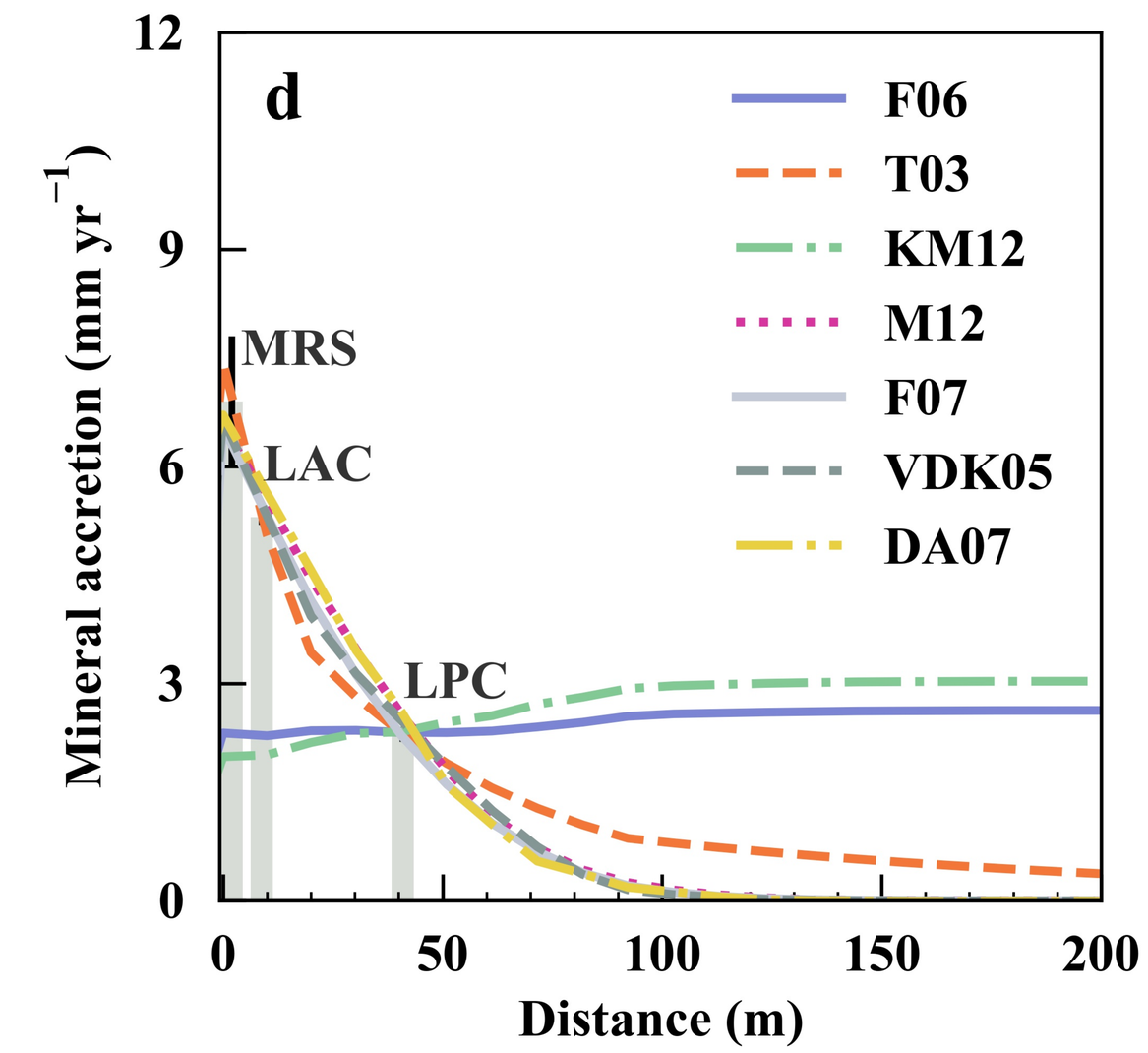
d
F06
T03
KM12
M12
F07
VDK05
DA07
MRS
LAC
LPC
Mineral accretion (mm yr^{-1})
12
9
6
3
0
0
50
100
150
200
Distance (m)

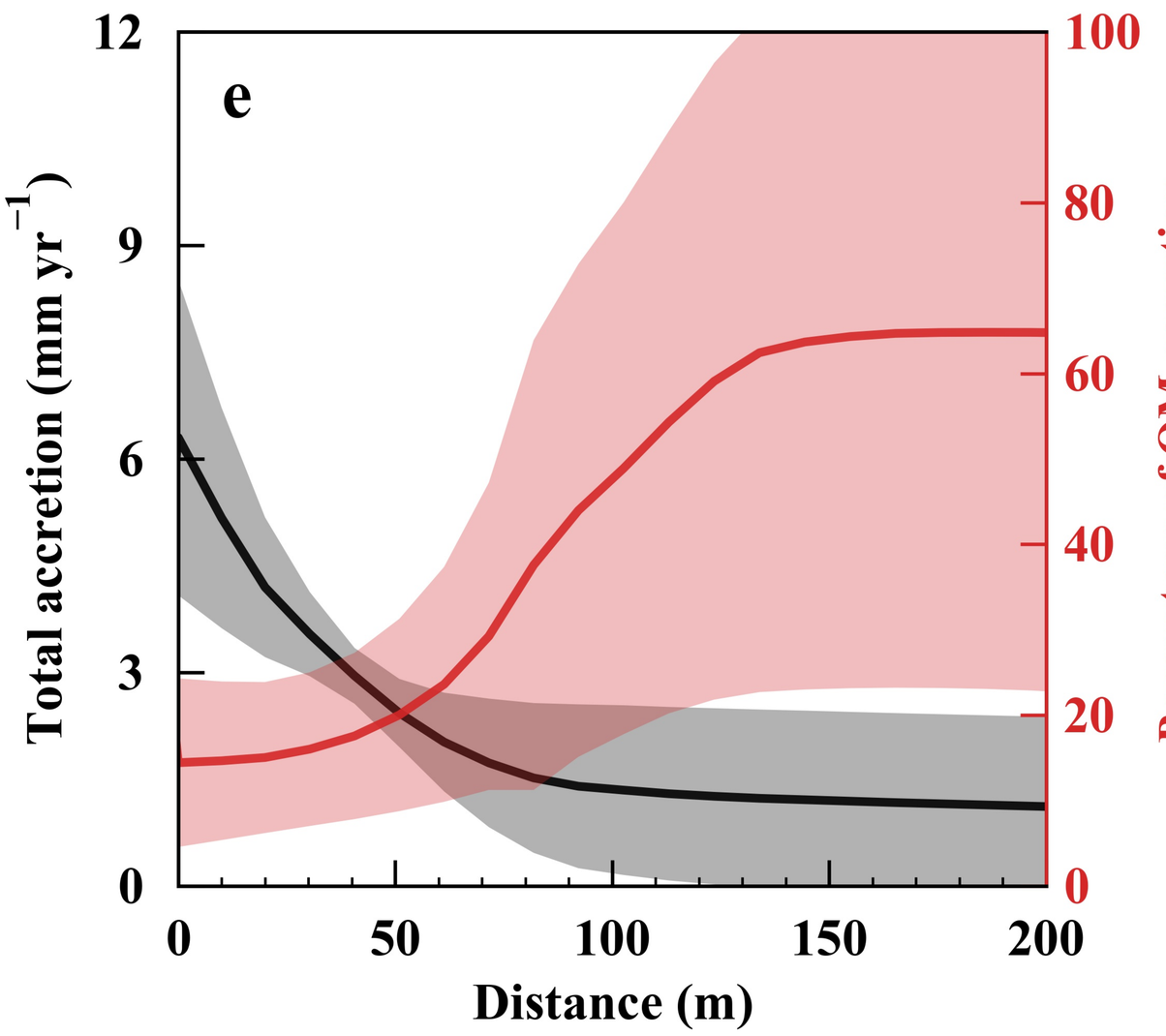
e
Total accretion (mm yr^{-1})
Percentage of OM accretion
12
9
6
3
0
100
80
60
40
20
0
0
50
100
150
200
Distance (m)

Figure 12.

a

M12
DA07
KM12
K16

Aboveground biomass (g m^{-2})

1600
1400
1200
1000
800
600

0
20
40
60
80

Distance (m)

b

M12
DA07
KM12
K16

OM accretion (gC m^{-2} yr^{-1})

250
200
150
100
50

0
20
40
60
80

Distance (m)

c

F06
T03
KM12
M12
F07
VDK05
DA07

Mineral accretion (mm yr^{-1})

50
40
30
20
10
0

0
20
40
60
80

Distance (m)

d

Total accretion (mm yr^{-1})

50
40
30
20
10
0

Percentage of OM accretion

100
80
60
40
20
0

0
20
40
60
80

Distance (m)